A FS pn-CCD detector for low background applications such as CAST

Master-Thesis von Philipp-M. Lang
December 2010

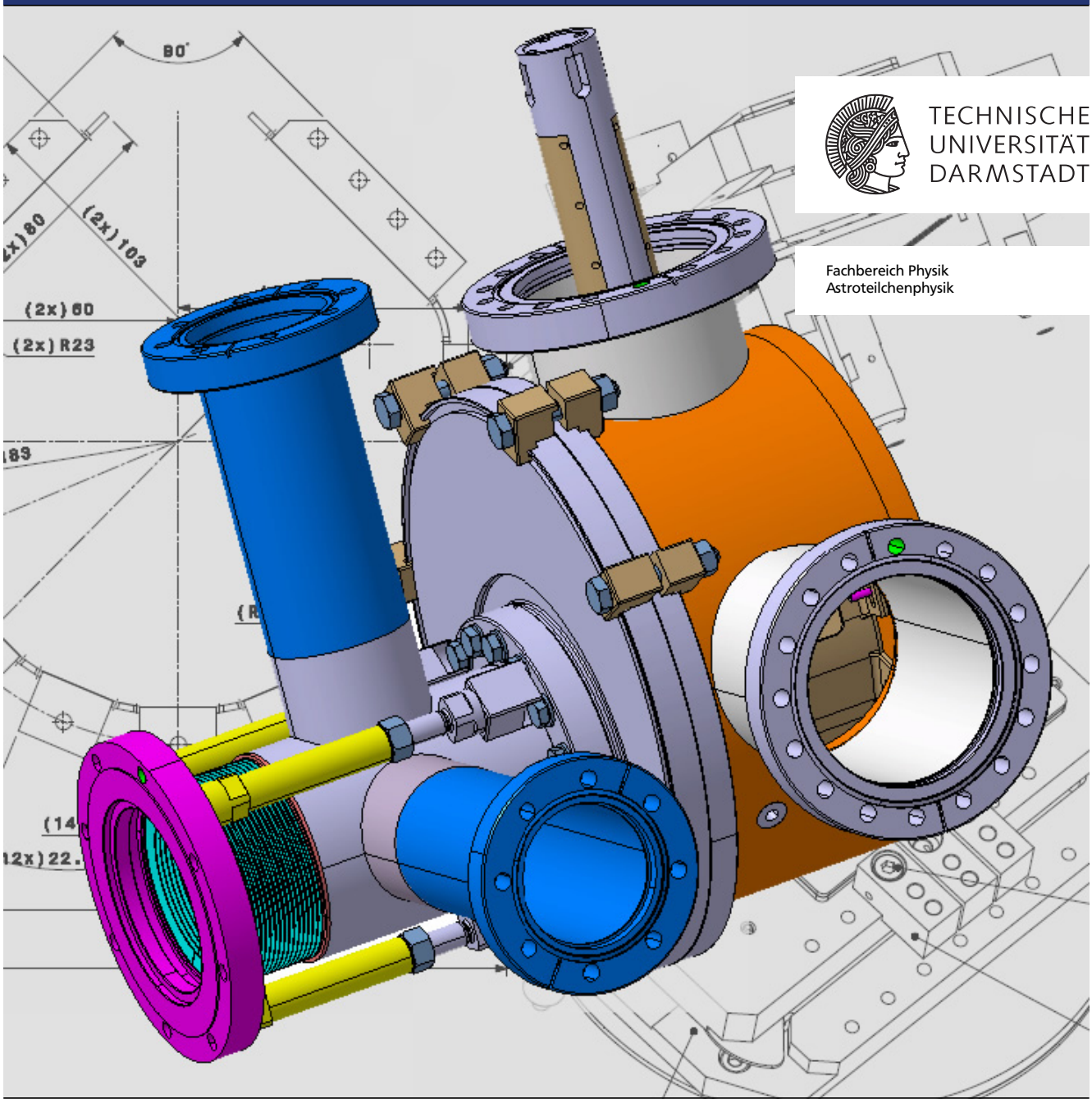

TECHNISCHE UNIVERSITÄT DARMSTADT

Fachbereich Physik
Astroteilchenphysik

A FS pn-CCD detector for low background applications such as CAST

Vorgelegte Master-Thesis von Philipp-M. Lang

1. Gutachten: Prof. Dr. Dr. h.c./RUS D.H.H. Hoffmann
2. Gutachten: Dr. M. Kuster

Tag der Einreichung:

Erklärung zur Master-Thesis

Hiermit versichere ich die vorliegende Master-Thesis ohne Hilfe Dritter nur mit den angegebenen Quellen und Hilfsmitteln angefertigt zu haben. Alle Stellen, die aus Quellen entnommen wurden, sind als solche kenntlich gemacht. Diese Arbeit hat in gleicher oder ähnlicher Form noch keiner Prüfungsbehörde vorgelegen.

Darmstadt, den 03. Dezember 2010

(Philipp-M. Lang)

Abstract

In experiments with a very low event rate, background is always a factor to be considered and hopefully to be reduced to get a clear signal. An example of such an experiment is the CAST experiment which searches for axions, possible candidates for dark matter.
This thesis gives an overview on the development of a new Framestore pn-CCD detector to fit the requirements of such experiments. General material composition and the working principle of a Graded-Z shielding concept for such a detector are explained. Exemplary simulations of such a shield and first test results for the detector's vacuum and cooling systems are presented as well.

Contents

List of Figures

List of Tables

1 Introduction

Many technical devices in our modern world would be unthinkable without CCD-sensors[1]. They are part of cameras and camcorders and play an important role in a wide range of physical applications.
In astronomy they took over the role of the formerly used photo plates as main imaging devices. Depending on their design they are sensitive over a wide wavelength range from infrared and visible light over the ultraviolet part of the electromagnetic spectrum to X-rays.
Satellite-based X-ray observatories like ESA's XMM-Newton or NASA's Chandra are equipped with X-ray sensitive CCDs, which cover energies from 0.1 keV up to approximately 15 keV with an angular resolution of about 0.5 arc seconds[2] [18]. Their high sensitivity enables them to detect even very faint X-ray sources.
CCD detectors are also frequently used in ground based experiments, e.g. in particle physics and astroparticle physics. One of these experiments is the CERN Axion Solar Telescope (CAST) at CERN, a helioscope that searches for axions, hypothetical particles which is a well motivated candidate for dark matter. Because the probability for the conversion of axions into photons is very low, the expected count rates in an axion detector are very low, too. For this reason very sensitive detectors and an effective background suppression are required.
In this thesis the development and construction of such a detector is described. The experience gained during the operation of the CAST X-ray telescope (which contains pn-CCD detector) was used to develop a significantly improved detector system.

The remainder of this thesis is structured as follows: In the first chapter a short introdcution into the theory of axions is given, followed by a review of the experimental method used in CAST to find evidence for the existence of the axion. After a general discussion about background sources of detectors in the CAST experimental environment, the requirements for a new detector are summarized and the general principle of operation of a CCD-sensor is explained.
An important point is the selection of materials for the components that are assembled in close proximity to the CCD-chip. As the count rate will be very low, the background has to be even lower, making it necessary to select these materials carefully regarding their intrinsic radioactivity and the energy of their X-ray fluorescence lines. This is further explained in chapter 4.
Special attention should be paid to the inner shielding, which employs a so-called Graded-Z Shield design. IXO[3], a future X-ray satellite, will be equipped with a similar Graded-Z Shield to protect its Wide Field Imager. Simulations of this shielding have been made with GEANT4 [2] in order to optimize it regarding its mass and the absorption of cosmic radiation.

[1] Charge-Coupled Devices
[2] This is for Chandra; XMM-Newton's resolution is around 5 arcsec but it has a larger effective area
[3] **I**nternational **X**-ray **O**bservatory. IXO could once be the successor of XMM-Newton and Chandra observing the X-ray universe.

Afterwards, the current status of the detector assembly is presented together with results from the first tests of the vacuum and cooling system.
Though originally designed as a backup detector for CAST or a future axion experiment, other fields of application for the detector are imaginable. These are mentioned in a short outlook at the end of this thesis.

2 The search for axions

2.1 Theory

The standard model of particle physics is a very successful theory that describes the elementary particles and three of four fundamental forces: electromagnetic interaction, weak and strong interaction. Yet it is not complete. For example gravity is not included in this theory at the moment. It contains three important symmetries:

- **C**: charge conjugation - exchange of particle and anti-particle
- **P**: parity inversion - reversal of space coordinates
- **T**: time reversal - direction of time is inverted

Symmetries are connected with conservation laws, but can be broken. Processes of weak interaction do neither conserve **C** and **P** separately nor their combination **CP**, for example. CP-violation was first observed by Cronin and Fitch 1964 in the decay of the neutral Kaon K^0 and its anti-particle $\overline{K}^0$ [10]. They discovered that K^0 and $\overline{K}^0$ decay in a slightly different way though matter and antimatter should behave exactly the same way. The reason is that neither of them are eigenstates of weak interaction, but a mixture of them.
In strong interactions all of these symmetries seem to be conserved, though Quantum Chromodynamics (QCD) postulates a breaking of CP-symmetry. This is apparent from the Lagrangian density of QCD, which can be written as

$$\mathscr{L}_{QCD} = \mathscr{L}_{pert} + \mathscr{L}_{\overline{\theta}} \quad \text{with} \tag{2.1}$$

$$\mathscr{L}_{\overline{\theta}} = \overline{\theta}\frac{g^2}{32\pi^2} G^a_{\mu\nu}\overline{G}^{\mu\nu}_a \tag{2.2}$$

where $\mathscr{L}_{\text{pert}}$ is a perturbative Lagrangian in QCD, $G^a_{\mu\nu}$ is the gluon field tensor and $\overline{G}^{\mu\nu}_a$ its dual. θ is a parameter describing the ground state of QCD-vacuum (often referred to as θ-vacuum) and $\overline{\theta}$ is θ with an additional term for weak interactions. It can basically take values of $0 \leq \theta \leq 2\pi$. A more detailed explanation can be found in [31] for example.
$\mathscr{L}_{\overline{\theta}}$ does not conserve CP-symmetry, which leads to a fundamental question: Why has CP-symmetry breaking of the strong interaction never been observed in an experiment?
If $\overline{\theta}$ was exactly zero, there would be no violation, but there is no obvious reason for that. If it was very close to zero, the violation effects would be very small and maybe not measureable yet.

$\overline{\theta}$ also plays a role in the calculation of the electric dipole moment of the neutron d_n.

$$d_n = 2.7 - 5.2 \cdot 10^{-16}\overline{\theta}\text{e cm} \tag{2.3}$$

Experimental results give an upper limit for $\left|d_n\right| < 2.9 \cdot 10^{-26}$ e cm (90% C.L.) [7]. This would result in $\overline{\theta} \leq 10^{-10}$. Of course this very small value is perfectly allowed but needs an explanation, since it would imply a fine-tuning of the terms that contribute to $\overline{\theta}$.
A possible solution for this problem was formulated by Robert Peccei and Helen Quinn in 1977 [21]. The fundamental concept of their approach is to make $\overline{\theta}$ a dynamical variable instead of a fixed parameter. In order to obtain $\overline{\theta} = 0$, they introduced a new symmetry, which is known today as the Peccei-Quinn-symmetry (or PQ-symmetry). This symmetry can spontaneously be broken resulting in a new particle they called "axion". It is a pseudoscalar massive boson, similar to the neutral pion π^0.
Besides solving the strong CP-problem, axions are a possible candidate for dark matter as their interaction with normal matter would very weak. Theories involving very heavy axions are already ruled out[1], but a light axion might be a solution when searching for the 23% of our universe that are predicted to be dark matter [34].
The inner regions of stars are a possible environment for the production of axions, so the strongest axion-source in our cosmic neighbourhood should be our Sun. There are several possible mechanisms of how axions can be produced. The most likely mechanism is via the Primakoff effect [23]. It describes how axions (or neutral mesons in general) can be produced by photons interacting with the Coulomb field of atomic nuclei. The Feynman-diagram of this process is shown in fig. 2.1.
Based on the Primakoff effect, it is possible to calculate the solar axion flux to $\Phi_a = g_{10}^2 3.75 \times 10^{11}\text{cm}^{-2}\text{s}^{-1}$. The differential flux is then given by

$$\frac{d\Phi_a}{dE_a} = 6.02 \times 10^{10}\ \text{cm}^{-2}\ \text{s}^{-1}\ \text{keV}^{-1} g_{10}^2 E^{2.481} e^{-E/1.205} \tag{2.4}$$

One can derive from this formula, that the mean axion energy is predicted to be 4.2 keV as shown in fig. 2.1 [4].

To detect axions one has to convert them back into photons. This is in fact possible under certain circumstances and is called inverse Primakoff effect. This effect requires a strong magnetic field the axions can couple to. The conversion probability strongly depends on the magnetic field strengh B and the length of the conversion volume L [8].

$$P_{a\to\gamma} = \left(\frac{g_{a\gamma}B}{q}\right)^2 \sin^2\left(\frac{qL}{2}\right) \tag{2.5}$$

q is the momentum difference between axion and photon and $g_{a\gamma}$ is the coupling constant for axions to photons, for which only an upper limit can be given at the moment. The best limit reached by the CAST experiment is $g_{a\gamma} < 8.9 \times 10^{-11}\text{GeV}^{-1}$. For axion masses less than 0.02 eV it supersedes the previous astrophysical limit based on the helium-burning lifetime of HB stars [4].

[1] Experimental limits have been set by the KEK experiment, for example [5].

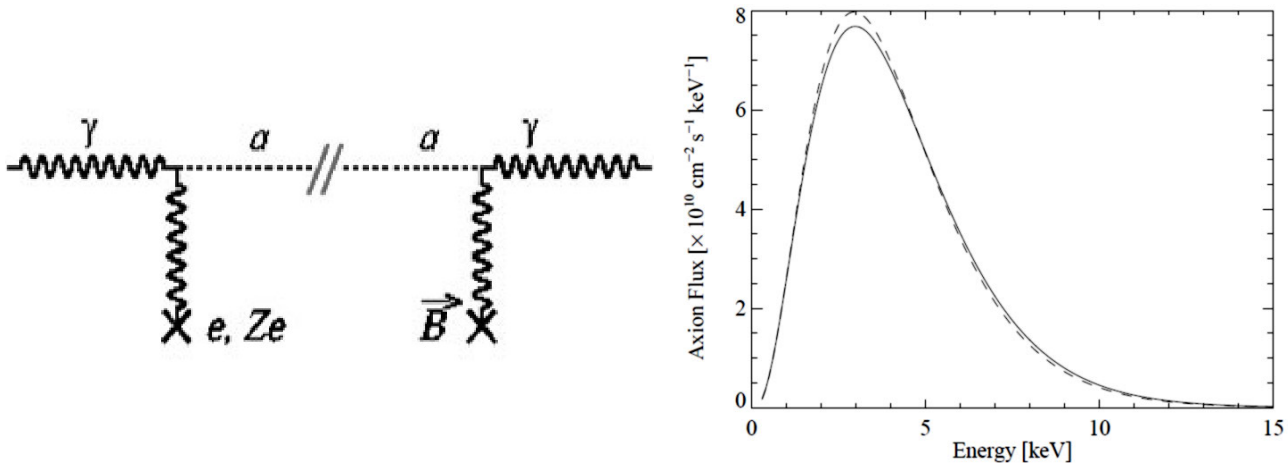

Figure 2.1.: Left: The Primakoff effect: A real and a virtual photon in the solar plasma couple to an axion; in a transversal magnetic field $\vec{B}$ it is converted back into photons. Right: The differential axion flux on Earth using two different solar models. (——) is recent solar model (2004) and (− − −) is based on the solar model from 1982 [6]. The maximum of the flux is around 3 keV, the mean energy $\langle E \rangle$ at 4.2 keV. [4]

2.2 The CAST experiment

The inverse Primakoff effect mentioned in the last section can be used to detect axions on Earth. One experiment that uses this effect is the CERN[2] Axion Solar Telescope (CAST). It is a so-called helioscope which searches for photons produced by axions that escaped from the Sun.
As eq. 2.5 shows, it is important to have a strong magnetic field over a distance as long as possible to get a satisfying conversion probability $P_{a\to\gamma}$. For this purpose CAST uses a superconducting magnet, a prototype of the magnets used at the Large Hadron Collider (LHC), that produces fields up to B ≈ 9 Tesla. The length of this magnet is L = 9.26 m [33]. As it was designed as an LHC magnet, which allows the collision of two beams, it has two tubes with a diameter of 43 mm each. For CAST this magnet is mounted on a turntable and a movable platform which can turn it ± 8° in vertical and from about 40° to 140° in azimuthal direction. This allows to follow the movement of the Sun for about 90 minutes in the morning and in the evening. The deviation from the Sun's center is less than 1 arc minute.
Basically one can install one detector at the end of each tube. On the one side data taking is possible in the morning while on the other side it is possible in the evening. Currently three Micromegas[3] detectors are installed, two at the sunset side and one at the sunrise side [1]. The fourth position illuminates an X-ray telescope with a CCD detector, which will be described later [17].
While not tracking the Sun the magnet is moved into a parking position and the detectors can take background data under the same circumstances as when following the Sun. This opens the opportunity to scan the background data for possible extrasolar axion sources that moved through CAST's field of view in that time, a project which is currently under investigation.

[2] Conseil Européen pour la Recherche Nucléaire
[3] **Micromes**h **Ga**seous **S**tructure

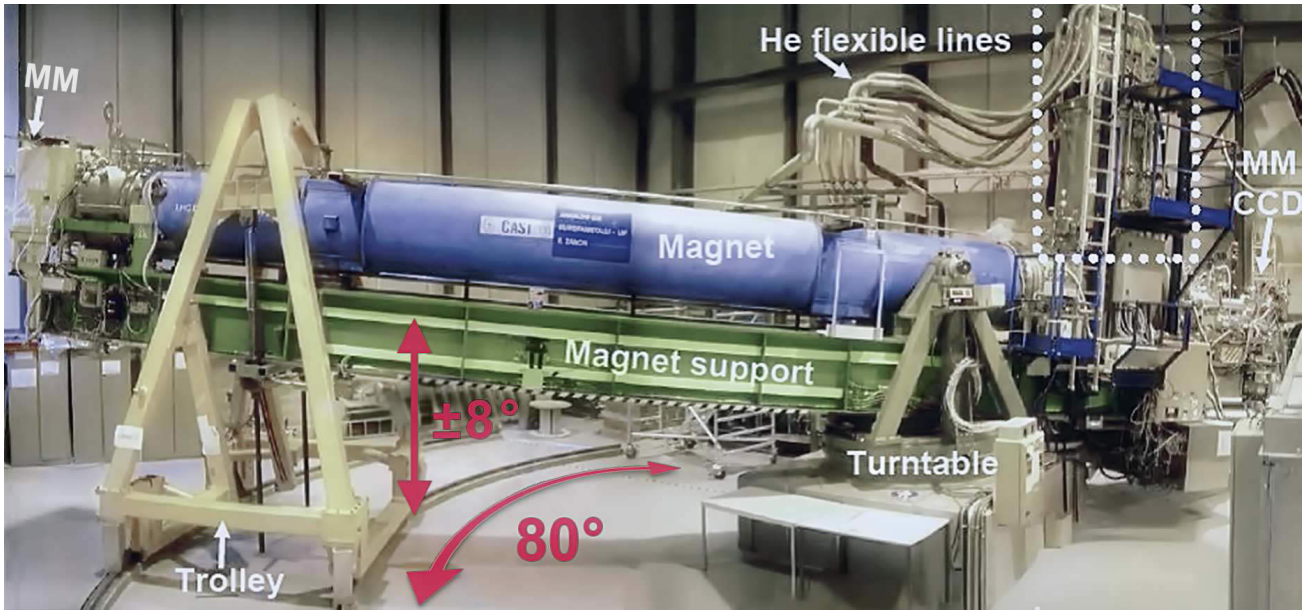

Figure 2.2.: The CAST experiment: The blue cylinder is a prototype for a superconducting LHC-magnet mounted on a turntable and a trolley. On the left side ("sunset side") two Micromegas detectors are installed, while on the other side ("sunrise side") one Micromegas detector and the CAST x-ray telescope are installed. The total weight of the experiment is about 40 t.

CAST is in operation since 2002. In *Phase I* (till 2005) [4], the tubes of the magnet were evacuated. When scanning for low axion masses ($m_a < 0.02$ eV), this is not a problem, but when moving to higher masses, axions and photons lose their coherence resulting in a decreasing conversion probability $P_{a\to\gamma}$. One can see this easily from eq. 2.5: If $q \cdot L \geq \pi$ the conversion probability will decrease. The momentum difference is $q = m_a^2/2E_a$.
It is possible to restore coherence in a short interval of axion masses by filling the tubes with a buffer gas. This lends an effective mass to the converted photons by changing the refraction index. A more detailed description can be found in [8]. To cover a wide mass range one has to change the pressure of the gas step by step.
In *CAST Phase II* ^{3}He and ^{4}He have been used as buffer gases. Using ^{4}He axion masses in the range $0.02\text{eV} \leq m_a \leq 0.4$ eV could be excluded. The upper limit for the coupling constant derived from ^{4}He is $g_{a\gamma} < 1.6 - 6.0 \times 10^{-10}\text{GeV}^{-1}$ (95% C.L.) for axion masses $m_a = 0.02 - 0.4$ keV [20]. The analysis of ^{3}He data is currently in progress and covers $0.4\text{eV} \leq m_a \leq 1.2$ eV.

On one end of the magnet's tubes a X-ray telescope is installed. As X-rays cannot be focused with lenses as easily as visible light for example, the telescope uses a different approach. A structure of concentric mirror shells uses the effect of total reflection of X-rays at grazing incidence angles. A combination of hyperbolic and parabolic surfaces can focus the rays on a single point. This setup is known as Wolter type I optics [32].
As the conversion probability from axions to photons is very low, such a telescope is very useful to get a better signal-to-noise ratio by focusing the X-rays on a smaller area. The telescope used

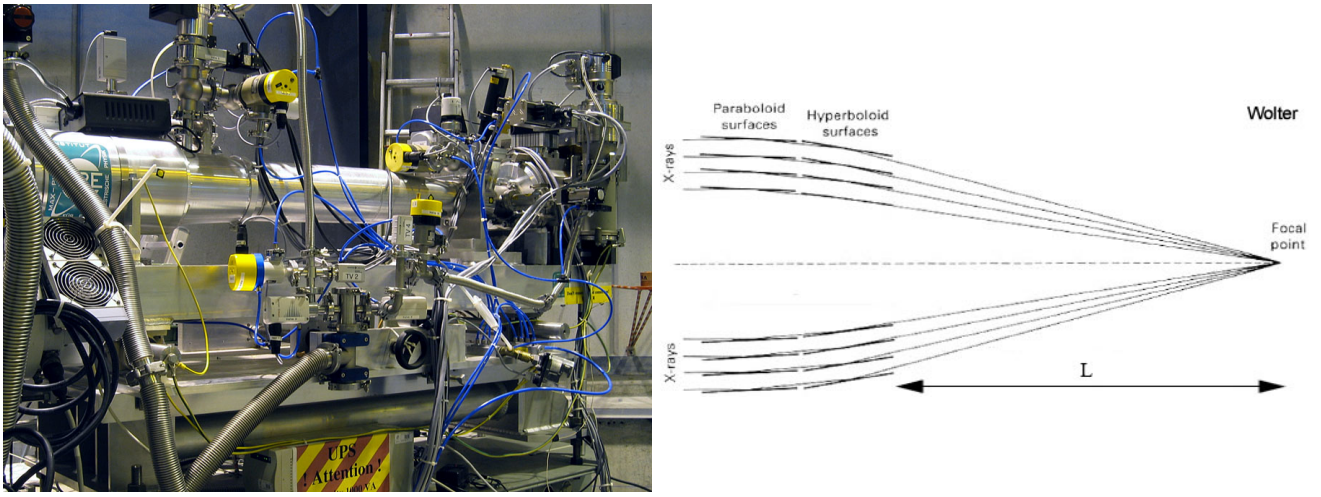

Figure 2.3.: Left: The X-ray telescope of CAST. The CCD detector is on the right side, the magnet on the left. Right: Total reflection first on a parabolic and then on a hyperbolic mirror shell is used to focus X-rays in a Wolter type I optics.

in CAST is a prototype for the ABRIXAS mission[4] [3]. It consists of 27 gold-coated nickel shells with a highly polished surface to focus incoming X-rays. By using this telescope, the signal-to-noise ratio could be increased by a factor of ≈ 154 [17].

The X-ray telescope illuminates a CCD, that is positioned in its focal plane. This is a pixelated silicon chip with 64 columns and 250 rows and was originally designed for XMM-Newton[5]. The energy range covered is between 1 keV and 7 keV. This is well around the expected mean X-ray energy from axion conversion of 4.2 keV. Nevertheless, a wider range would be desirable. However, this is difficult due to some fluorescence lines from system components used near the CCD such as the Cu-K_α-line at 8 keV (for example due to the cooling mask made of copper).
Even so, the X-ray telescope is currently the most sensitive detector used at the CAST experiment with a background count rate of $\approx 8 \times 10^{-5}$cts cm^{-2}s^{-1}keV^{-1} (which is roughly one event every three hours per cm^2 and keV) [9]. This was achieved after adding an internal copper shielding within the vacuum chamber around the CCD.
Probably due to metal abrasion acumulated on the surface of the CCD, the first chip was damaged by a short circuit in 2005. The second one currently in use is the last copy of this chip design available. If it was damaged, no spare parts would exist. This is one reason for the plans within the CAST collaboration to construct a new CCD detector.
The functional principle and the additional advancements of a new CCD compared to the old one will be described in Chapter 4.

[4] A Broadband Imaging X-ray All-Sky Survey; a satellite based X-ray observatory that should map the sky in X-rays from 0.5 to 15 keV.
[5] X-ray Multi Mirror - XMM-Newton is one of ESA's most successful X-ray observatories in space

3 Background studies

3.1 Radiation interactions with matter

When trying to describe the background characteristics of an experiment correctly one has to take into account several effects caused by many different particles. Not all are important for every experimental setup, of course. For the applications mentioned in this thesis, the most important particles are protons, electrons and photons. Their energy has to be high enough to cause ionization. This means for photons taht their energy must be in the range of X-rays or gamma-rays.
Anyways, when designing a shielding for background-reduction, it is imporant to have in mind the processes how these particles interact with matter. As the interaction-processes are basically the same in ground based applications and in space environment they will be discussed together before explaining the specialities of the background on Earth and in space separately. In both environments X-ray sensitive CCDs are in use and there are similar shielding-concepts for them though the background is quite different.

A CCD is a semiconductor detector that can basically detect any kind of radiation such as electromagnetic radiation, electrons, protons or any other particles that are able to ionize matter and thereby strike out electrons while moving through the detector.
There are two important ways how electromagnetic radiation can transfer energy to the electrons in the detector material. The first one is by the **photoelectric effect**. This means that a photon is completely absorbed by an electron in an atomic shell. Because the atomic nucleus is needed as collision partner to conserve momentum, this is not possible for free electrons. The cross section for the absorption of a photon in the K-shell is particularly large because the nucleus as third collision partner is very near (assuming a photon energy E_γ which is high enough for this ionization process).
As a consequence of this hole in an inner shell, a bound electron from an outer shell can fill it. This causes the emission of characteristic X-rays with an energy equal to the difference of the energy levels of these shells. For an electron falling from the L- to the K-shell this characteristic energy is known as K_α-line (if it came from the M-shell it would be named K_β-line and so on). However, this energy can also be emitted in form of an electron from an outer shell. This is known as an *Auger electron*. Its kinetic energy is normally quite low compared to the primary photoelectron.

Another important effect is **Compton scattering**, the scattering of photons off electrons. In this case, a photon transfers only a part of its energy to an electron and thereby changes its momentum. This also causes ionization.

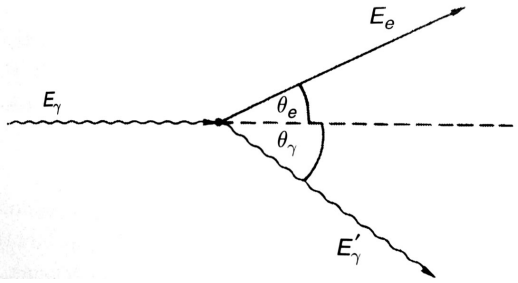

Figure 3.1.: Compton scattering of a photon with initial energy E_γ off an electron. (Source: [11])

The energy loss of the photon can be calculated as

$$E'_\gamma = E_\gamma \cdot \frac{1}{1 + \epsilon(1 - \cos\theta_\gamma)} \tag{3.1}$$

with E'_γ and E_γ beeing the final and initial energy of the photon, respectively, and $\epsilon = E_\gamma / m_e c^2$. This shows that photons scattered under an angle of $\theta_\gamma = \pi$ transfer the most energy to the electrons. The probability for Compton scattering per atom of the absorber increases linearly with the atomic number Z, since it is dependent on the number of electrons available [16].
It should also be noted that the contrary effect can occur, meaning the scattering of high-energetic charged particles off low and high energy photons. This *inverse Compton scattering* plays an important role in the description of several phenomena in astrophysics [11].

A third important process is **pair production**, the production of an electron-positron pair. It can only occur at energies above $2 \cdot m_e c^2 = 1022$ keV, since this is twice the electron's rest energy. The positron now can annihilate with another electron, causing the production two photons with an energy of 511 keV that can interact with the surrounding material again.

Besides that, also the produced electron (and other charged particles as well) can interact with matter in the detector. By **impact ionization** an electron can free other electrons off an atomic shell as shown in eq. 3.2. This can cause an avalanche of electrons like it is used for amplification in Geiger counters.
The incident electron can also leave the atom in an excited state and thereby cause the emittance of photons. This is known as **impact excitation**. The mechanism is shown in eq. 3.3.

$$A^Z + e^- \rightarrow A^{Z+1} + e'^- + e''^- \tag{3.2}$$

$$A^Z + e^- \rightarrow A^{*(Z+1)} + e'^- \tag{3.3}$$

Other effects like Rayleigh scattering, where a photon does not lose energy, or the interaction of neutrons with matter, are of minor interest. More details can be found in [11]. Some particular effects for applications important for this thesis will be mentioned in the next two sections.

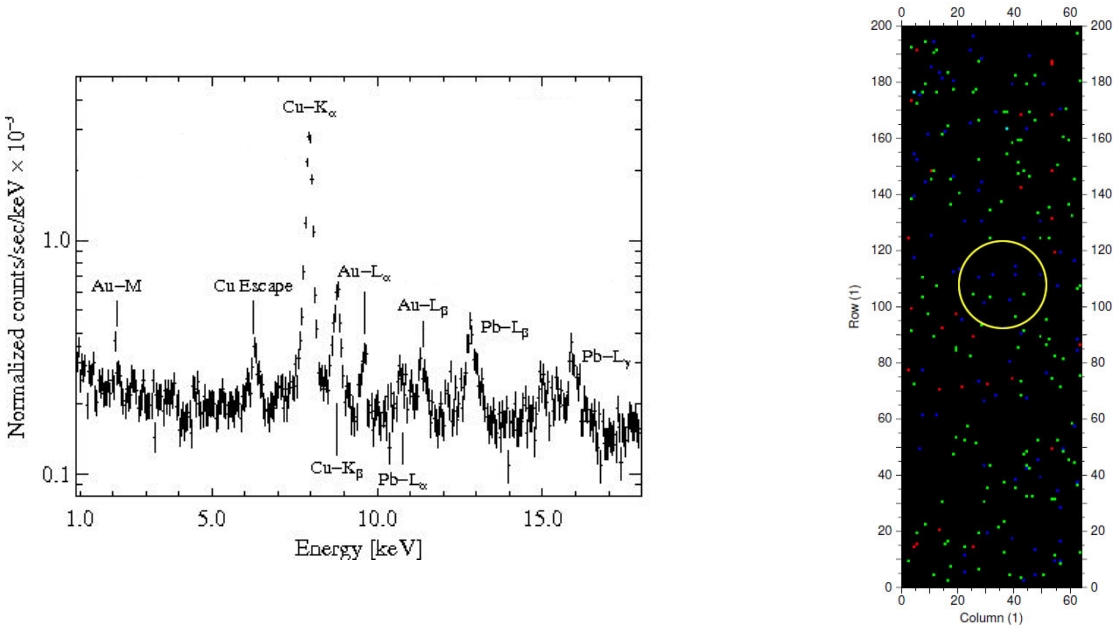

Figure 3.2.: Left: A typical CAST background spectrum taken in 2007. Several prominent X-ray lines are produced by materials close to the CCD chip, mainly Pb, Cu and Au (Source: [4]. Right: An intensity image of the events during a one-day background measurement on the CCD. Different colours of the points stand for different energies. The yellow circle marks the focal area of the X-ray telescope.

3.2 Background studies for CAST

To reduce the background for an experiment, the most important thing is to understand its sources. For CAST we are in the lucky situation to have the collected background data of several years of runtime. It allows us to take many problems into account, that limited the sensitivity of the detector, when designing a new one in order to improve the sensitivity. A detailed study of the background of the present CAST pn-CCD detector can be found in [9] and [25].
While not looking at the Sun, the CAST magnet is moved into its parking position. This time is used to take background data under the same conditions as during solar observation. It is also possible to take background data *while in solar observation mode*. As the illuminated field of view of the CAST X-ray telescope (which is limited by the magnet's aperture) covers only a fraction of the whole CCD, one can focus on the data taken by the pixels not illuminated as another source of background data (see fig. 3.2). Both data sets, the data taken in the parking position and the data taken outside the illuminated area during solar observation, have been taken into account for the analysis of the background. Fig. 3.2 shows a typical background spectrum of the CAST CCD taken in 2007.

As one can see, the spectrum shows fluorescence lines of those elements built in near the CCD. This mainly refers to an outer lead shielding (resulting in the Pb-L line) and an inner copper shielding and parts of the cooling system that consist of copper and also gold. The energy range below 1 keV is dominated by the Cu-L$_\alpha$ line (0.930 keV) and possibly the oxygen K-line at 0.525 keV (not shown).
But what excites these fluorescence lines? There are a few main components that contribute

to their excitation: One source can be cosmic rays, or more precisely, their secondary products. Another one is natural radioactivity in the experimental hall's walls and air, and a last one is the intrinsic radioactivity from the detector materials themselves.
The last two groups are caused by primordial radioactive impurities, mostly the isotopes ^{40}K,^{232}Th, ^{235}U and ^{238}U.
Detailed measurements of the intrinsic radioactivity of the detector parts were made at the Canfranc Underground Laboratory using an ultra low background germanium spectrometer. An accurate measurement of all walls in the experimental hall in different heights were done with a germanium detector at CERN. Additionally the radon concentration in the air has been measured over a long time period. The mean activity caused by radon is assumed to be $\sim$10 Bq m^{-3} [9].
Relevant decay products of cosmic rays are muons and neutrons. While muon interactions can be rejected with almost 100% efficiency due to their long ionization tracks, neutrons are a different matter. As neutron production induced by muons is strongly enhanced in high Z materials - such as the lead shielding - they might contribute to the background significantly.
Table 3.1 gives an overview of how these factors contribute to the overall counting rate. These results were derived by Monte-Carlo simulations with GEANT4[1] using the measurements mentioned above as input information. As the neutron flux for example has not been measured in detail, it is assumed to be similar as the neutron flux on sea level, which has already been measured [15]. Thus it was possible to determine the CCD's response and counting rate for those background sources.
Unfortunately one of the main intrinsic sources of background is the ceramics the CCD chip is attached to. To reduce this part is very difficult, so one has to concentrate on the other components to reduce the background.

Table 3.1.: Contribution of different background sources to the CAST CCD detector's counting rate between 1 keV and 7 keV. All differential fluxes are given in units of counts cm^{-2} s^{-1} keV^{-1} and (Source: [9]).

Detector Component	**Mean Differential Flux**
CCD Board	$(5.83 \pm 0.41) \times 10^{-7}$
CCD Chip[1]	$< 2.20 \times 10^{-5}$
Ceramics	$(1.17 \pm 0.14) \times 10^{-6}$
Sockets	$(1.34 \pm 0.15) \times 10^{-6}$
Front and Rear Cooling Mask	$< 6.21 \times 10^{-7}$
Other Factors	
Walls	$2.81 \pm 0.16 \times 10^{-5}$
Radon	$\sim 1 \times 10^{-6}$
Interactions with neutrons	6×10^{-6}

[1] This is only an upper limit. A more accurate measurement of the chip's differential flux is difficult because of its low mass.

[1] GEANT4 is a toolkit for simulating the interactions of particles with matter, based on Monte Carlo methods

3.3 Background in space

The environment in space is completely different compared to the environment on the ground, where we are protected by Earth's atmosphere and its magnetic field. But there are some concepts of shielding that work in ground based experiments and on-board satellite missions, too. X-ray sensitive CCDs and similar semiconductor detectors are in operation in both environments. The International X-ray Observatory (IXO) is a mission jointly pallend by NASA, ESA and JAXA together. IXO's Wide Field Imager is a semiconductor detector[2] As done at CAST it will use a Wolter telescope to focus incident X-rays and similar methods of background reduction. This is the reason why this work will focus on both of them.

In space as well as on Earth, (charged) particles and electromagnetic radiation have to be taken into account. Neutral particles would mainly be neutrinos, which - though present in large numbers - would interact with a spacecraft not at all, or neutrons, which alone are not stable and would decay into protons (their lifetime is $\sim$ 15 minutes). Electromagnetic radiation is only a problem if it is energetic enough to ionize matter in the spacecraft or the detector itself. Of course, if the energy is to high and an interaction unlikely, the radiation will also just pass through.
This leaves charged particles as a main source of background. Cosmic radiation mainly consists of protons ($\sim$ 98%) and a smaller fraction of He nuclei and electrons. Elements with higher Z are also present, but their flux is almost negligible. For the simulation results presented in Chapter 5 only the protons will be considered.
One can easily determine a main source for this proton radiation, which is our Sun. It ejects the so-called solar wind, mainly consisting of protons, from its surface. The presence of this wind is measurable in our whole solar system up to the heliopause, the theoretical borderline where it is stopped by the interstellar medium. Protons from sources outside of our solar system have also to be considered and contribute to the background. How strong this contribution is, depends on the intensity of the solar wind and the strength of the solar magnetic field which varies over time.
This variation is mainly caused by the 11-year solar cycle, a periodic fluctuation, that was first discovered by counting the number of sunspots on the Sun's surface. In the minimum of the solar cycle the Sun is "quiet" and no or just a few sunspots can be seen, while in its maximum, there can be hundreds of them. A quiet Sun corresponds to a lesser flux of solar protons, yet the overall proton flux is rising. This is because more extrasolar protons can enter the heliosphere.
Of course the flux measured on a satellite also depends on its position in the solar system. The further away from the Sun the more extrasolar protons will dominate. For Earth orbit the spectrum of these particles is known very well. If one wants to place an observatory in one of the Lagrange points[3], this spectrum might differ slightly because the distance to the Sun varies and Earths magnetic field does not deflect the particles. As there are no accuate radiation measurements at L2, the intended position for IXO, and since the distance from Earth to L2 is very short compared to the distance from Sun to Earth ($\approx$ 1%), we will use the CREME96 model as input information for the simulations. This model is stated be valid to the Mars orbit.

[2] DEPFET as an acronym for *Depleted P-Channel Field Effect Transistor*. More information can be found here: [27].

[3] Langrange points (also called Libration points) are those positions, where gravitational forces of two celestial bodies (Sun and Earth for example) cancel each other (in a rotating coordinate system)

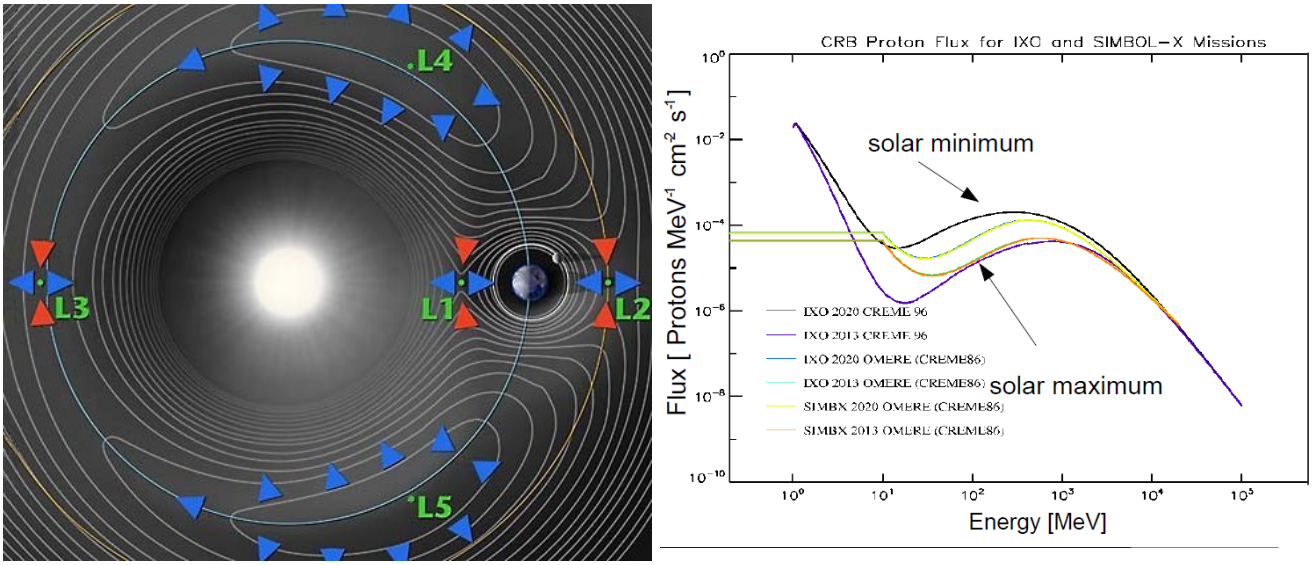

Figure 3.3.: Left: Location of the Libration points in the Sun-Earth system. The contour lines show the gravitational potential of a test mass in the commen gravitational field of the Earth and Sun in the co-rotating reference frame. L4 and L5 are stable equilibrium positions, while the others are unstable (Source: NASA). Right: Estimated proton fluxes for the SIMBOL-X and IXO missions during different times of the solar cycle. Partly the CREME86 model is used. The more recent one is CREME96 [30].

CREME96[4] is a suite of programs that allows the creation of numerical models of the ionizing radiation environment in near Earth orbit and its variation over time. The needed spectra for IXO are based on this software (see fig. 3.3). They are used as input spectra for the simulations shown in Chapter 5.

[4] **C**osmic **R**ay **E**ffects on **M**icro-**E**lectronics

4 Development of a new detector

One important reason for the development of a new detector for CAST is to have a spare detector if the current CCD fails. This fatal problem occured in late 2005, probably because metal abrasion caused a short-circuit on the CCD's surface.
Constructing a new detector provides the chance to include new concepts for background reduction and optimization, based on the knowledge gained during the years of operating the actual one. Since also CCD fabrication techniques have improved during the last years, there are new CCD technologies available with improved performance. The so-called FS-CCD[1] is a product of this evolution and will be described in the next section.
Table 4.1 shows some characteristics for the present and the new CCD detector. A more datailed description follows in the next section.

Table 4.1.: Comparison of some important characteristics of the new and the present CCD. Especially the lower background rate and the extended energy range are important for CAST.

	present CCD	**FS pn-CCD**
number of pixels	64×200	256×256 (+FS-area)
pixel size	150×150 μm^2	75×75 μm^2
energy range	0.5 - 20 keV	0.1 - 20 keV
energy resolution	180 eV	140 eV
background	8×10^{-5} Cts s^{-1} cm^{-1} keV^{-1}	$< 2 \times 10^{-5}$ Cts s^{-1} cm^{-1} keV^{-1} [1]
quantum efficiency[1]	> 0.9	> 0.9

[1] This is an estimation and not yet measured

[2] The quantum efficieny is energy-dependent. The given numbers are valid for an energy range between 1 and 8 keV.

4.1 A Frame-Store pn-CCD

Charge-Coupled Devices (CCDs) are a special kind of pixelated semiconductor detectors. To understand their working principle, one has to understand some characteristics of semiconductors in general.
A pure semiconductor has the same number of (free) electrons and holes. Considering the band structure of a semiconductor, there is only a small energy gap ($\sim$ 1 eV[2]) that separates the conduction band from the valence band. This makes it easy for electrons to be excited into the conduction band allowing them to move freely through the material. The atoms now have an excess of positive charge, often simplified as a positively charged "hole".

[1] A so-called Frame-Store pn-CCD has an additional storage area.

[2] for Si the gap is 3.6 eV at room temperature if phonon excitations are taken into account

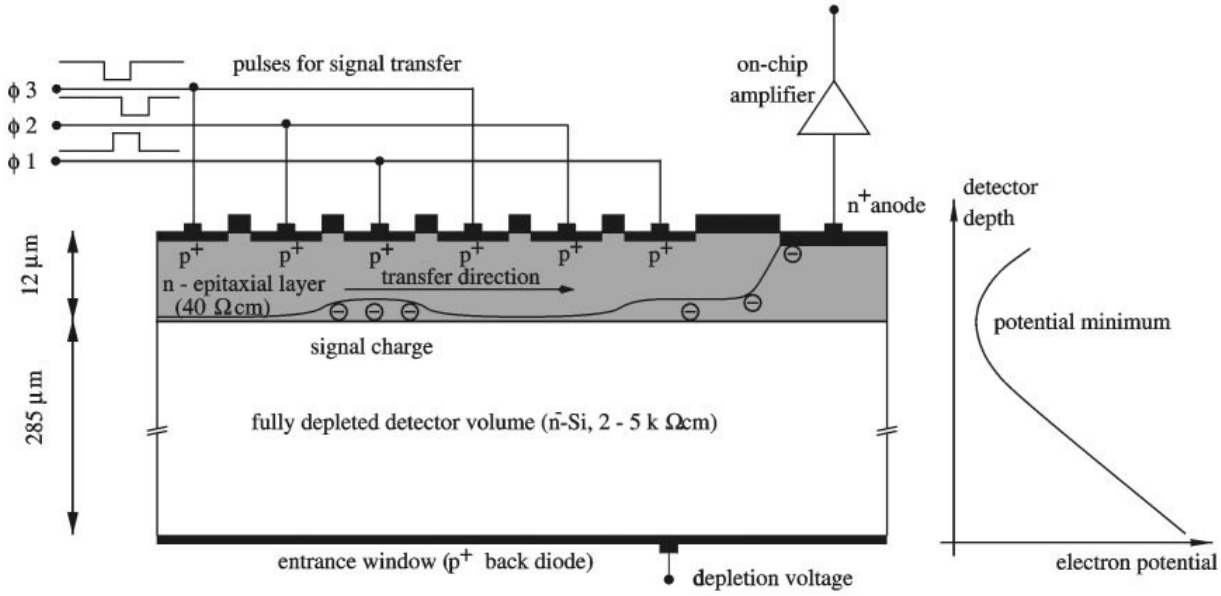

Figure 4.1.: A schematic cross section of a pn-CCD along a transfer channel. The signal charge is transferred to the anode in a potential well by varying the potentials ϕ_1, ϕ_2 and ϕ_3. The device is backside illuminated and fully depleted over 300 μm (Source: [26]).

Typical semiconductors used in detectors are silicon or germanium. One can change the properties of such a semiconductor by adding impurities to the material. Usually this is done by adding small amounts of trivalent or pentavalent atoms - elements of the third or fifth main group in the periodic table for example. This process is known as doping. Doping with trivalent atoms leads to p-type semiconductors, which incorporates some additional "holes" in the material, while doping with pentavalent atoms leads to an excess of electrons, so-called n-type semiconductors. Typical materials for p-type doping are phosphorus, arsenic and antimony and gallium, boron and indium for n-type semiconductors.
When placing a p-type semiconductor on the surface of an n-type semiconductor, electrons will start to diffuse from the n-type side towards the p-type side, filling the holes there. This goes on until the diffusion is in equilibrium with the drift of the charges caused by an Electric field that is generated by the accumulated charges on either initially neutral side of the junction. As the diffusion and drift current now cancel out, this leads to a depletion zone around the junction.
If an ionizing particle enters the depletion zone, it creates electron-hole pairs. Because of an additional external electric field, they will be swept out of the depletion zone. By applying electrical contacts on both sides of the depletion region, one can detect these electrons either directly or store the electrons in a potential well for later read-out. The latter one is done in CCDs and other pixelated detectors.
CCDs are read out by shifting these charges across the pixel structure. Using three transfer registers with potentials ϕ_1, ϕ_2, ϕ_3, one can first collect the charges in potential wells, and then transfer them through the other pixels in that column towards the edge of the pixelated structure. By using the right cycle time one can read each pixel-row step by step. For the CAST CCD the read-out time is $t_{read} = 6.06$ ms.

Unfortunately, this operation brings along some disadvantages. While shifting the charge through the pixels, two problems occur. First, some charge lost during the transfer from one pixel to another, resulting in a charge transfer inefficiency, or in other words the charge transfer efficiency (CTE) is smaller than 1 (CTE < 1). For the CCD currently in use, the CTE is around 99.96%. When shifting through n pixels, the charge arriving at the anode is

$$q_{anode} = q_n \cdot \mathrm{CTE}^n \tag{4.1}$$

The second problem occurs, when another particle hits the detector and produces additional charges during the read-out procedure. Those charges can, in transfer direction, not be allocated to the right pixel. These so-called *out-of-time events* account for about 8.1% of all events in the configuration used at the CAST experiment [31].
This problem is can be significantly reduced using a next-generation CCD: a Frame-Store pnCCD. In addition to the imaging area, where the charges produced by incident particles are collected, this kind of device provides a storage area with an equal number of pixels. This area is shielded against X-rays. After a given integration time, the full image is transferred very quickly to the Frame-Store area, where it is read out row by row as described above. In this time a new image can already be collected.
For the FS-CCD designated for use in our detector (originally designed for the ROSITA X-ray satellite) the pixels in the image area have a size of $75 \times 75\ \mu\mathrm{m}^2$. The storage pixels are smaller with a size of $75 \times 50\ \mu\mathrm{m}^2$. The transfer time from one area to the other is only $100\mu\mathrm{s}$ [19].

The quantum efficiency (QE) of the CCDs, both the FS-CCD and the present CAST CCD, is very high (> 90%) over a wide energy range (see fig. 4.1). The QE is the percentage of photons of a certain energy that hit the detector and are really detected as events.
Fig. 4.1 shows that the QE rapidly decreases above a certain energy (∼8 keV for the present CCD). The main factor that is limiting the QE at higher energies is the thickness of the silicon chip (or more accurate the depletion depth, which is 450 μm for the FS-CCD). For a larger depletion depth, the probability for an interacting of a high energetic photon would increase. For the CAST experiment this is not really of concern, since photon energies above 14 keV are not of interest.
On the low energy side, several factors are limiting the efficiency of the CCD. One is the dark current from the CCD and the noise. To reduce it, the CCD has to be cooled, so that the number of thermally generated electrons decreases. For the CAST CCD the dark current is minimized at temperatures around -130^{o}C. The FS-CCD will operate at full performance at a temperature of -60^{o}C or close to this value. Nevertheless, it is necessary to cool the chip in both cases.
Also the material of the thin entrance window becomes important for low energy photons, as they might lose a part of their energy or be absorbed before entering the depleted area.

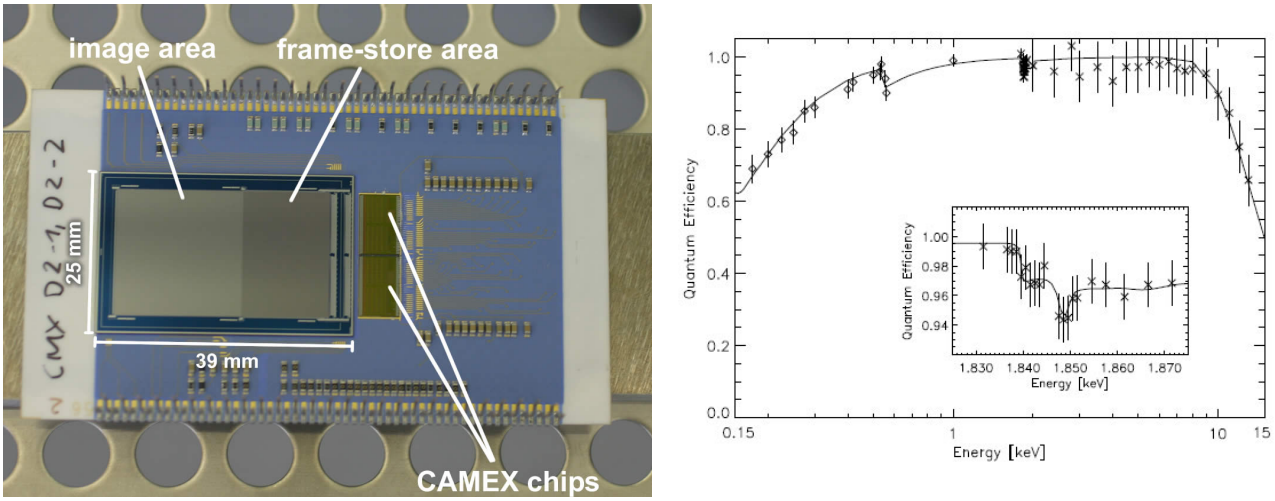

Figure 4.2.: Left: The FS pn-CCD detector. Frame-Store and image area are coloured in different shades of grey. On the right side one can see the two CAMEX-chips for read-out. Right: The quantum efficiency of a 300 μm thick pn-CCD. It is above 95% in the energy range that is of interest for CAST. Dips in the quantum efficiency curve are caused by the oxygen-K edge at 0.525 keV (from the SiO_2 entrance window) and the silicon K-edge at 1.84 keV from the detector itself (Source: [26]).

4.2 Choice of materials

The selection of materials for the detector vessel and components surrounding the CCD is very essential for the background counting rate. The reasons for that can be summarized in three main aspects.

- The intrinsic radioactivity due to impurities of ^{40}K,^{232}Th, ^{235}U, ^{238}U and ^{210}Pb has to be very low.
- Other impurities might be a problem as well, as they might cause unwanted fluorescence lines. One example is oxygen, for example in form of oxidizations on the surfaces. This has to be watched carefully, since oxygen produces a fluorescence line at 0.525 keV, which lies in the favored energy range between 0.5 and 8 keV.
- Fluorescence lines have to be shielded or have to lie in an energy range outside the favored energy range.

The last point is considered by implementing a so-called Graded-Z shield design, which is explained in detail in the next section.
For the first point, one has to select materials with a low intrinsic radioactivity. For example one can select old lead that was stored underground and thus contains a low fraction of unstable ^{205}Pb. This is used as solder for the *PCB-Board* which will carry the CCD. There is no gold coating on the board, as this would cause an Au-M X-ray line in our background spectrum, similar as seen in fig. 3.2.
All copper components like the cooling mask and the heat pipes are made of almost oxygen-free copper. After cleaning them for their application in vacuum, they were stored in a vacuum storage chamber, in order to prevent oxidization. The pressure in the storage chamber was

$p < 1$ mbar. This was also done to protect the polished surfaces. Those are important to ensure a good thermal contact.

The most challenging problem was to find a sufficient carbon-rich material, which is necessary for the innermost layer of the Graded-Z Shield. Several plastic materials were considered, each with its own advantages and disadvantages. The material has to contain as little other elements besides carbon and hydrogen as possible and it has to resist the low temperatures near the detector. This also means that the thermal expansion coefficient[3] of the plastic must not differ too much from the surrounding copper an aluminum components to prevent mechanical stress. Table B.1 gives an overview about some possible materials.
Because some screws out of such a material are needed to carry the weight of other components inside the vacuum vessel, it is required that they do not fracture at low temperatures. For the screws we chose Polyamid 6.6 (PA6.6) because these were the only adequate plastic screws available. As their lower working temperature is considerably above the temperature the cooling system will provide, we tested their stability at low temperatures by cooling them with liquid nitrogen (boiling point 77.36 K). Even after several cooling cycles their stress resistance was quite acceptable. The test results are presented in Appendix B.
The innermost layer of the Graded-Z Shield is made of HDPE[4]. Kapton would be a sufficiently good alternative but its water absorption is quite high and it is much more expensive.
The spacers that hold the PCB-Board an keep the Radiation Shield in place are made of PEEK (polyether ether ketone). PEEK has the advantage of a low water absorption and a low thermal expansion coefficient while having a high mechanical load capacity. There are several types of PEEK with additional components of glass fibre or carbon fibre to increase load capacity or conductivity or other material properties. We chose pure PEEK for the spacers. Spare parts are made of PEEK GF30 (PEEK with 30% glass fibres added) for testing purposes.

4.3 Concept of a Graded-Z Shield

The Graded-Z Shield is one of the main innovations for the new FS-CCD detector. An additional shielding made of copper for example would introduce fluorescence lines in the X-ray spectrum. As this cannot be prevented, one has to choose the material in a way that the newly introduced fluorescence lines do not lie in the preferred energy range for the measurements with the detector. Unfortunately materials with low-energy fluorescence lines are poor absorbers for X-rays with higher energies. A Graded-Z Shield provides a solution for both the absorption of high energy X-rays and the absorption of fluorescence lines that lie in the energy range one wants to measure in.
Graded-Z refers to the number of protons "Z" in an atom, that characterizes each element. The layers of such a shield consist of materials with decreasing Z from the outside to the inside. This order is chosen because with decreasing Z, the energy of the fluorescence lines also decreases. The energies of some emission lines are shown in table 4.2 for some selected elements.
Of course when choosing the elements, one has to consider the presence of K_β and L-lines for elements with higher Z as well.
Another important point is, that high Z materials absorb high energetic X-rays better than those

[3] This material specific coefficient sets the temperature T of a material in relation with its expansion: $\Delta L \approx \alpha_T \cdot L_0 \cdot T\ \alpha_T$.

[4] **H**igh **D**ensity **P**oly**e**thylene, $\rho = 0.94\text{g/cm}^3$ (for low density PE $\rho \approx 0.92\text{g/cm}^3$)

Table 4.2.: Energies of the fluorescence lines for some elements used in Graded-Z Shields. The K_α-line energy increases with increasing Z. This is just meant to give an overview, so the slight difference between $K_{\alpha 1}$-lines and $K_{\alpha 2}$-lines is not taken into account. Data is taken from [29].

Element	**No. of protons Z**	**K_α-line** [keV]
carbon	6	0.277
aluminum	13	1.486
copper	29	8.04
tin	50	25.2
tantalum	73	57

with a small number of protons. The consequence is clear: One has to use high Z materials to absorb the hard X-rays and low Z materials to absorb the fluorescence photons emitted by the high Z materials - a Graded-Z Shield.
For the purposes of CAST the shielding consists of three layers: copper, aluminum and PE. A transmission curve for X-rays is shown in fig. 4.3. The way it is integrated into the detector design is somewhat special, as there is no seperate layer structure as one would expect when thinking of the designs of some X-ray observatories in space. Some parts are not exclusive to the Graded-Z Shield at all, but also serve other purposes such as the Copper Cooling Mask, which is on the one hand partially the copper layer of the Graded-Z shield, but on the other hand also responsible for cooling the chip. The aluminum layer is a Radiation Shield surrounding the complete inner parts of the detector and covered on the inside with plates of PE.

4.4 The complete detector

All components explained in the previous sections finally must be integrated into the detector system. A first assembly was made during November 2010, including the vacuum system and the thermal system. The CCD and most parts of the read-out electronics were not included at that time, because they are not needed for the first tests of the vacuum and thermal system. The performance of these systems in test runs is shown in Chapter 6.
The central part of the vacuum system is a copper vessel that will later hold the CCD under a pressure of about $p \approx 5 \times 10^{-6}$ mbar. Its interior is shown in fig. 4.4. On top of the vessel a Ricor 535 Stirling Cryocooler is mounted. It is connected via two krypton-filled heatpipes with the Cooling Mask of the CCD to provide the necessary -130^{o}C working temperature. Two other heatpipes are connected with the Radiation Shield, that serves as a cold trap with a slightly lower temperature than the CCD. This keeps water from condesating on the sensitive chip.
On the right side of the copper vessel is a feed through for the connection to the read-out electronics.
On its front side a flange leads to the turbopump of the vacuum system, and via a flexible bellow to the X-ray telescope if mounted at the CAST experiment.

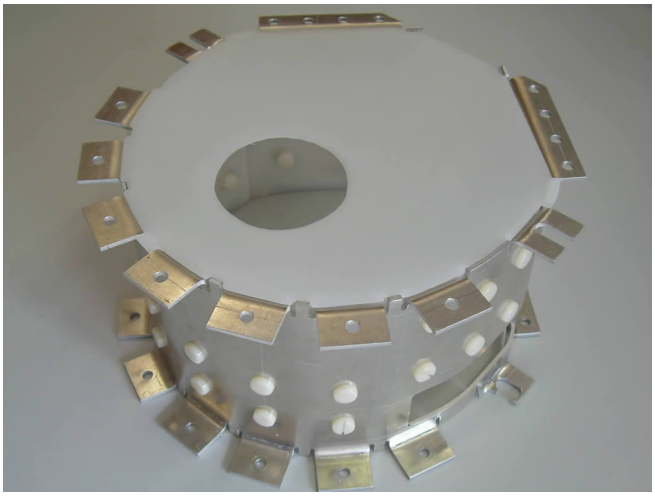

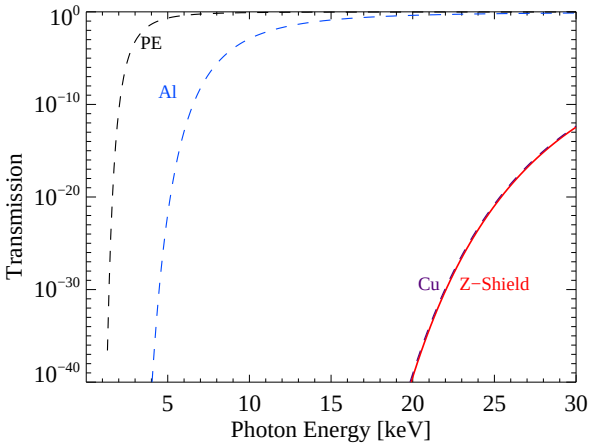

Figure 4.3.: Left: The Radiation Shield made of aluminum with a cover of PE. On the inside one can see the inner layers, also made from PE. They are held in their position by plastic screws. The field of view is visible as a hole in the shielding, allowing X-rays, that hit the detector coming from the CAST magnet and X-ray telescope, to pass. Right: The transmission for X-rays for a Graded-Z shield and its layers consisting of 1 mm of PE, 1 mm Al and at least 3 mm Cu.

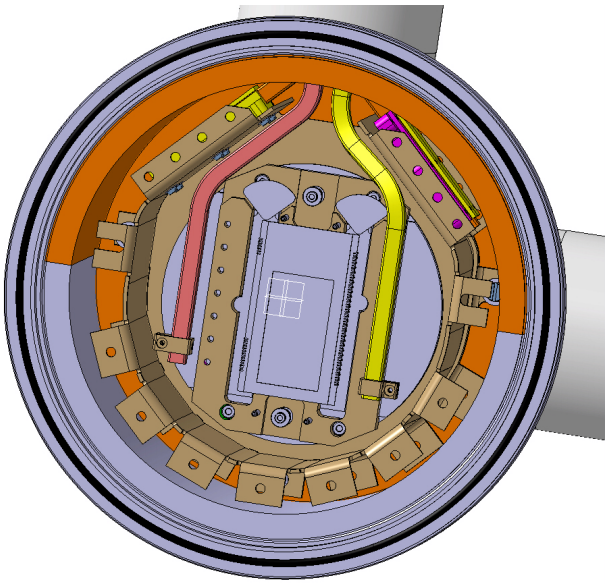

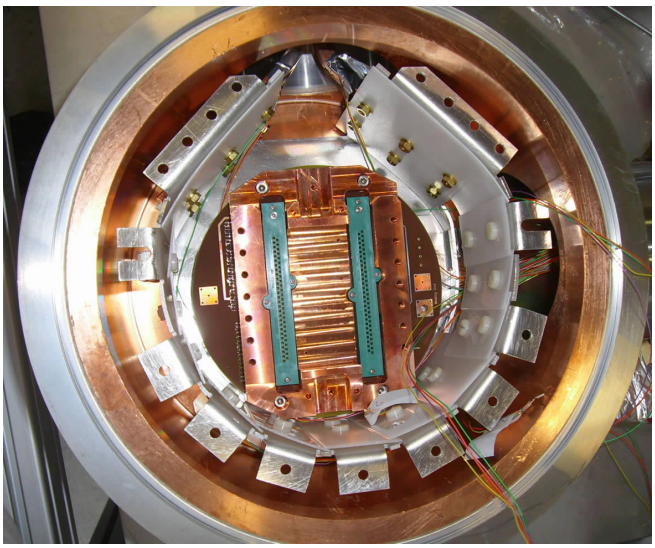

Figure 4.4.: Left: A image from a 3D model of the detector's interior. Radiation Shield and Cooling Mask are coloured brown. The heat pipes are marked in red and yellow. Right: The same view in reality. The green sockets in the center are the connections for the CCD, surrounded by the Cooling Mask. The varicoloured cables belong to several PT100 thermal sensors.

5 Simulations for the Graded-Z-Shield

5.1 Simulations with GEANT4

How effective a Graded-Z Shield works, cannot be determined easily. An increased thickness for the layers will absorb primary X-rays better, but in return might produce more secondary particles (mainly electrons and gammas), which increase the background count rate.
To optimize such a Graded-Z Shield before even constructing it, one can use simulation toolkits such as GEANT4 [2]. GEANT4 uses the Monte Carlo condensed random walk approach to simulate the passage of particles through matter. It is based on the C++ programming language. Originally it was developed at CERN for the simulation of processes in high energy physics, especially the events in particle accelerators such as the LHC at CERN.
Further improvements and the addition of new libraries and physics models made it interesting for applications in astrophysics and space engineering as well. One can use GEANT4 to simulate the effects of solar and cosmic radiation on hardware aboard spacecrafts or on humans exposed to that radiation.
Possible particles for simulations are gammas, electrons, protons and almost every other particle relevant for particle physics. Their initial direction of flight and their initial energy spectrum habt to be defined as input parameters.
Detectors, shieldings and other kinds of matter can be placed in the GEANT4 environment by building a geometry out of simplified geometric objects (cubes, cylinders, etc.) and specifying the material's properties. One or more of these objects can be classified as sensitive region, from where data about particle interactions and impacts can be read out.
When running a GEANT4 program the movement and interaction processes for each particle are simulated step by step one after another. Thus the execution of the programme can be devided into three levels: The steps of a single particle through the so-called *World Volume* (the framework for our geometry) are the lowest level. All steps together until the particle is absorbed or leaves the world volume are one event. The whole simulation run consists of all events together.
Any information about the tracked particles can be written out at any time for further analysis, allowing to follow tracks, get estimates for deposited energy, get the response of a detector or test the efficiency of a shielding.
Yet there are some limitations for GEANT4. For example it is not possible at the moment to simulate the long term activation of materials that are hit by energetic particles without external code [14].

5.2 Simulating the International X-ray Observatory's Graded-Z Shield

One important point to keep in mind when designing a spacecraft is that it has to be as light as possible. Every additional kilogram of payload costs extra money for launching the rocket that will bring it up into space.

When thinking about shieldings for a detector onboard a satellite this is very important as such a shielding might become unnecessarily heavy if its thickness is not optimized. So one important task is to find a balance between the thickness of a shielding and its weight.
Another problem is that a thicker Graded-Z Shield produces more secondary particles when exposed to the cosmic radiation. The most important secondary particles are electrons and gammas. Thus another task is to find an optimum between the production of secondaries and the absorption for (primary) X-rays. Fig. C.6 motivates the necessity of a Graded-Z Shield for suppressing fluorescence emission from components in detector proximity and the importance of accounting for secondary electrons.
A GEANT4 simulation was written to analyze these effects on different layer configurations. Though developed to simulate the Graded-Z Shield for the International X-ray Observatory IXO, the code is also useful for other Graded-Z Shields like the one of the FS-CCD detector. One needs only to change the layer materials and thicknesses and the input spectrum. This can be done very easily, because all these parameters are changeable via a single macro file. Thus it is not necessary to recompile the program each time the geometry is changed.
It was essential to keep the geometry as easy as possible. More complex geometries would require more time for the simulations as they are computationally intensive. Since one has to simulate several different layer configurations, this would be very time-consuming. The only other way would be to reduce the number of primary particles which would lead to an increasing statistical uncertainty.

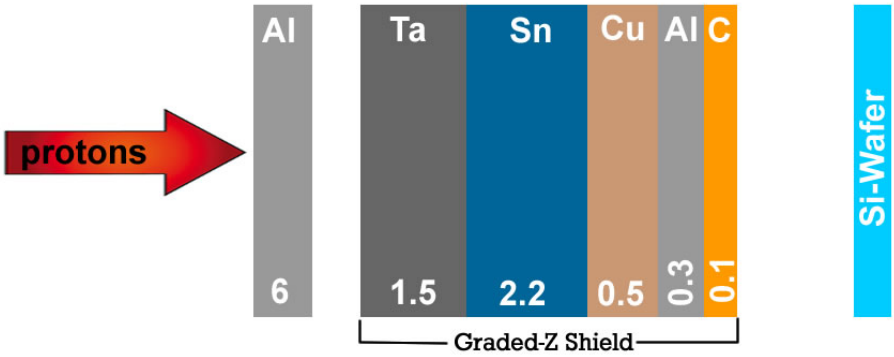

Figure 5.1.: Schematic overview of the configuration of the Graded-Z Shield for IXO. The thicknesses are given in mm in the lower part of each layer (as derived from the first draft for the shielding). The distance from the innermost layer to the Si-Wafer is 20 mm. The outermost aluminum layer does not belong to the Graded-Z shield but simulates the spacecrafts structure. The wafer's thickness is 450μm and its width and length 10 cm each. The structure of the entrance window is included in the simulations but not shown in this scheme.

All simulations use an input spectrum derived from a CREME96 model for L2 during a solar minimum (see fig. C.1). The number of primary particles is 1 million protons for each simulation run. As discussed before, other particles are only a minor factor in the composition of the cosmic radiation and hence not included.
Early simulations done by Steffen Hauf showed that far more electrons than gammas were produced as secondary particles. The main source of these electrons was the tantalum layer [12].

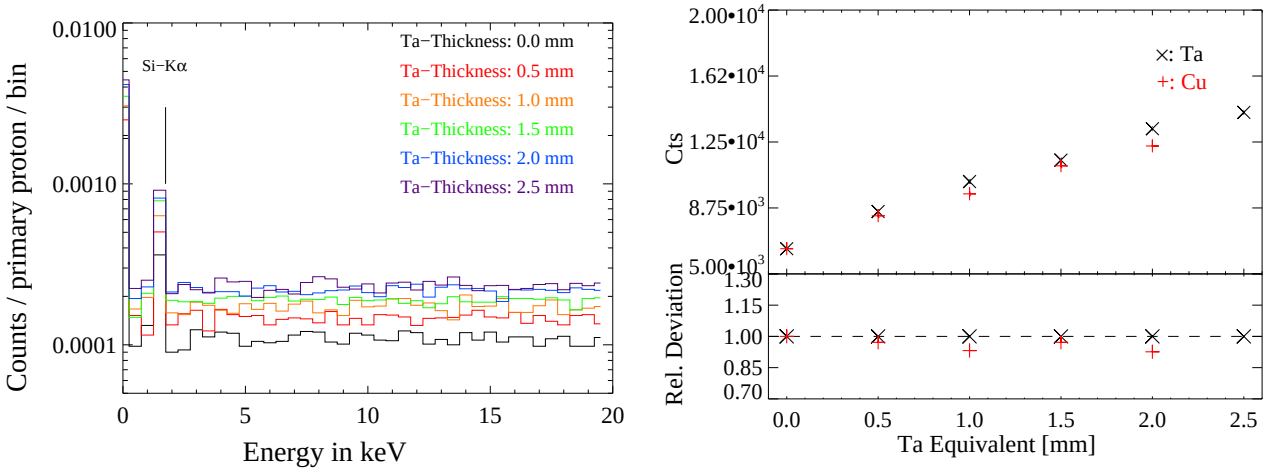

Figure 5.2.: Left: The gamma energy spectrum for a Graded-Z with tantalum layers of different thicknesses after irradiation with 10^6. The Si-K_α line is the only prominent line in the spectrum. The binsize is 0.5 keV. Right: A comparison of the number of counted gammas below 20 keV between simulations with tantalum and simulations with their density-equivalent in copper. The lower half of the plot shows the deviation of the counting rate with copper relative to tantalum. Errors have not been plotted as they would lie within the size of the symbols.

Because of that, first the thickness of the tantalum layer was varied in steps of 0.5 mm. As the Graded-Z Shield becomes much more transparent for X-rays then, this was compensated by increasing the thickness of the copper layer.
Since the density of copper is much lower than that of tantal ($\rho_{Cu} = 8.92$ g/cm^3 and $\rho_{Ta} = 16.65$ g/cm^3), a thicker layer of copper is needed to provide the same absorption as a tantalum layer. The ratio is:

$$\frac{\rho_{Ta}}{\rho_{Cu}} = 1.867 \tag{5.1}$$

In other words, 0.5 mm tantalum correspond to 0.934 mm copper. Nevertheless, the absorptivity of particles is slightly different though the areal density is the same.
The counting rate of gammas with energies below 20 keV is always lower when using copper instead of tantalum. This trend is the same for the electrons. The detailed results are plotted and tabulated in Appendix C.
The gamma spectrum clearly shows the Si-K_α peak, which cannot be suppressed by the Graded-Z Shield, since this line is caused by the Si-Wafer that has been used as detector itself. The electron spectrum shows a small peak around 1.5 keV whose origin still has to be determined, but apart from that it is also flat.

The electron flux resulting from the layers of the Graded-Z Shield is about one order of magnitude higher than the gamma flux, and the proton flux is not much below the electron flux. According to this, electrons and protons would be the main contributors to the background.
But there is a way to reduce that by using a software filter. X-rays that hit the detector in the direction of the X-ray telescope will deposit their energy only within a very small number of

pixels, since the generated cloud of electrons will not spread much wider. Particles with higher energies or with another direction will cause larger charge clouds or long ionization tracks through several pixels. One can exclude such events by using a pattern recognition algorithm. This provides the possibility to exclude all events that deposit energy in more than N = 4 pixels because they would not be caused by X-rays. Since pattern recognition was not included for the Graded-Z simulations presented here, it is just referred to [13] and [28] for further information.

To prove the validity of the simulations setup, we varied the input parameters in two different ways. One way was by modifying the angle of the proton beam relatively to the orientation of the Graded-Z Shield. As one can see from table 5.1 this angle has a high influence on the number of gamma rays that hit the detector.
The other way was by adding a bismuth germanate (BGO) layer between the Graded-Z layers and the outer alumin layer. BGO is part of the shielding of the high energy X-ray detector that is installed in close proximity to the WFI and hence be relevant for the Graded-Z design as well. This additional layer increases both gamma-flux and electron-flux significantly.
Both observations will be investigated with further simulations.

Table 5.1.: A comparison of the count rates for different particles with different initial parameters. The standard simulation includes the layer thicknesses as shown in fig. 5.1. In the second one, the proton beam hits under an 45^o angle. The third one has an additional layer of BGO between the tantalum layer an the outer aluminum layer.

Particle type	**Standard simulation**	**45^o angle**	**additional BGO layer**
electron	241968	276153	484416
gamma	11472	8054	48547

6 System tests of the FS-CCD-Detector

6.1 Vacuum system

The FS-CCD detector's vacuum system is designed to create a vacuum in the order of 5×10^{-6} mbar. It is possible to vent the system with nitrogen by providing liquid N2 in a Dewar vessel through a flexible Teflon-tube and a particle filter attached to V3 (see fig. 6.1).
The copper vessel is sealed with a DN250 Viton O-Ring[1] with an aluminum centering ring and a spacer ring. All other flanges on the HV side are CF-type flanges and are sealed with copper rings. The only exception besides the copper vessel's flange itself is a flange designed as connection to the X-ray telescope, which is a ISO-K-type flange and also sealed with a Viton O-ring.
Additionally, a feed-through for the CCD's power supply and read-out electronics is provided on one side of the copper vessel. The Stirling cooler is connected on top of the vessel.

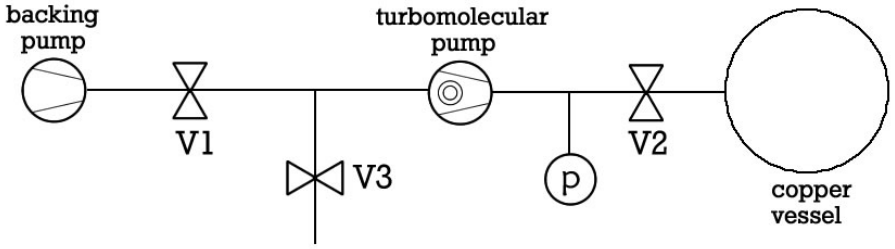

Figure 6.1.: The vacuum system for the FS-CCD detector, which will be installed in the copper vessel. V1 and V2 are standard valves. V3 is a venting valve. At "p" the pressure is measured using a Active Pirani/cold cathode transmitter.

To ensure a proper operation, the vacuum system has been tested in several configurations. The system was completed step by step. First tests have been made with only the T-piece and the pressure sensor connected to test the performance of the turbomolecular pump and the absence of leaks at the T-piece and valve V2. The minimal pressure was $p = 1.2 \times 10^{-7}$ mbar.
Of course with each flange connection added, the system is more prone to leaks. The latest measurements with the full system applied show a minimal pressure of $p = 4.8 \times 10^{-6}$ mbar, which is well in the range of the designated pressure of $p = 5 \times 10^{-6}$ mbar. The average leak rate[2] was 1.59×10^{-5} mbar s^{-1} (see fig. 6.2). One reason for this quite high leak rate could be a small leak caused by scratch on one of the flanges of the T-piece. It was probably damaged during assembly, and now might be a source of a small leak. This still has to be checked. However, the vacuum is more than sufficient for a performance test of the cooling system.

[1] Viton® is a brand of synthetic rubber often used for O-ring seals

[2] this value is not yet normalized to the volume of the vacuum vessel since the exact volume is difficult to calculate. The volume of the copper vessel is around 5 l and the rest of the system might be another 2.5 l, which leads to a leak rate $\approx 1.2 \times 10^{-4}$ mbar l s^{-1}

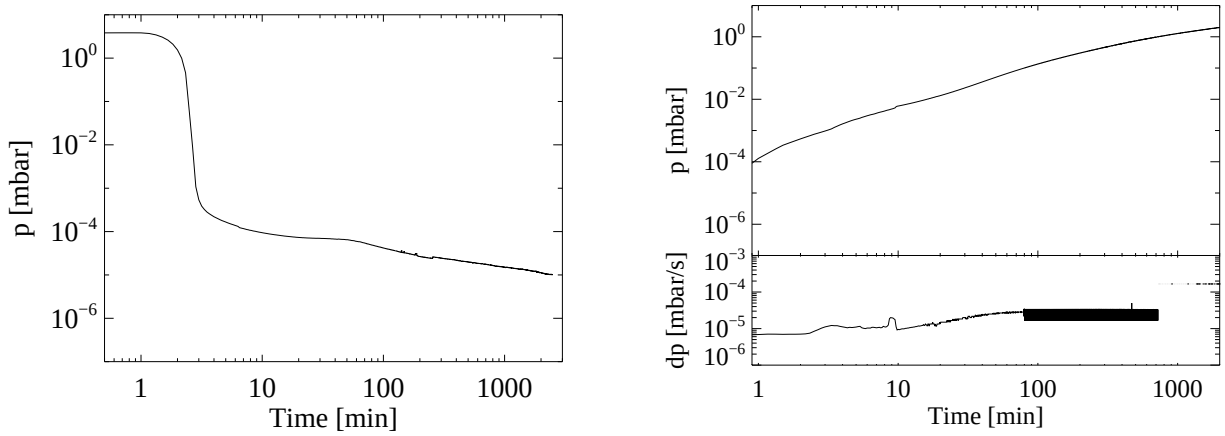

Figure 6.2.: Left: Plot of the pressure measurements during the evacuation of the vacuum vessel. Both axes uses a logarithmic scale, since irregularities are clearly visible this way. Right: Plot of a leak rate measurement (closed valve V2). The upper part of the plot shows the pressure and the lower part its change over time.

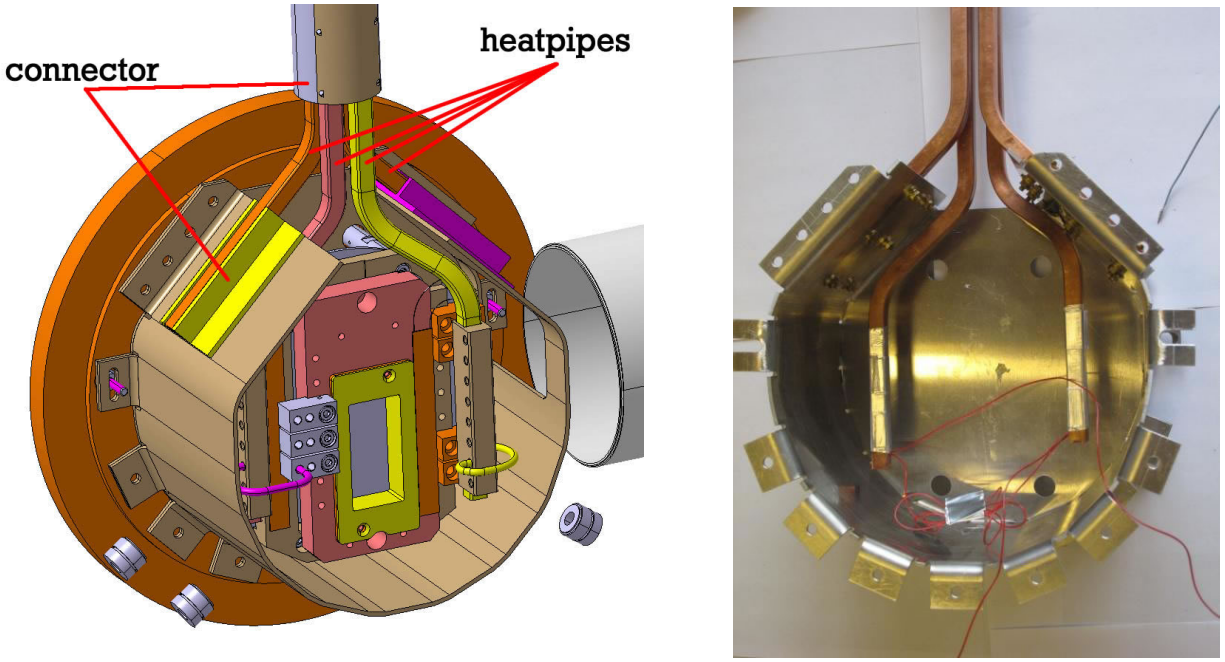

Figure 6.3.: Left: Image of the detector's interior. The heatpipes and their connectors are marked. At the current status, they are not connected to the copper cooling mask (red block in the center), because the connection braids are still to be fabricated. Right: The cooling system as it was assembled for testing at CERN in Feb. 2010 [22].

6.2 Cooling system

The detector's cooling system cools the CCD to its working temperature at -60 ^{o}C. The cooling power is provided by a Ricor 535 Stirling Cooler. The layout of such a cooler is very similar to a Stirling engine. A short overview about the working principle is given in [24].
The head of the cooler is connected to four krypton-filled heatpipes, that allow an efficient heat transfer. These heatpipes are made of copper as well as their connecting pieces to the other components: By choosing the same material for both parts no mechanical stress or a loss of thermal contact can occur due to different thermal expansion coefficients of the materials.
Two of the heatpipes are connected to the Radiation Shield. The other two will transfer the heat from the Copper Cooling Mask where the CCD is located. They are not yet connected to the cooling mask since the copper braids for that still have to be produced.
To provide an optimal thermal contact, the heatpipes' surfaces are polished and the tolerance of their fittings to their connectors are very low. Fig 6.3 shows the cooling system's design.
A first test of the system was done in Feb. 2010 at CERN [22] showing that the system reaches its specifications. The maximum temperature difference ΔT between the head of the Stirling Cooler and the connections to the Radiation Shield was less than 4 K. The cooldown took about 5 hours starting at ambient temperature. Fig. D.2 shows a plot of the temperatures during the cooldown.
To make sure that the system is still functional after the transport from CERN to Darmstadt and a repolishing of the surfaces of the heatpipes, the cooling system's test has to be repeated at TU Darmstadt. This time the cooling system is integrated properly into the copper vessel together with the Radiation Shield and the PCB-Board. This was not possible at CERN, since the copper vessel was not ready for testings until summer 2010. A plot of a first measurement for the performance of the cryocooler is shown in fig. 6.4. The cooler reaches its minimal temperature of T = 120 K (a standard value for test purposes) after about 3.5 hours.
Yet the performace of the heatpipes in the complete setup is not tested until now. For these performace measurements, several PT100 temperature sensors are placed on the heatpipes, the connector to the cold finger and the Radiation Shield. This work is in progress.

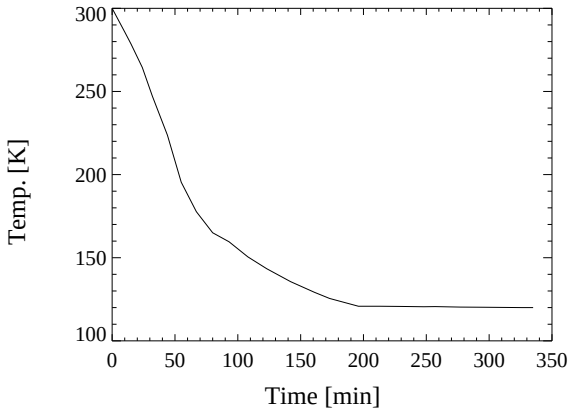

Figure 6.4.: A performace test of the Stirling Cooler done at TUD in Nov. 2010. The temperature is measured with the cooler's internal sensor at the cold finger. No damages or output losses seem to have occurred since the last tests at CERN.

7 Outlook

As shown in the previous chapter, the vacuum system works as expected. The thermal system has shown its capability to reach its specifications at CERN, but this still has to be confirmed after its transport and its integration in the copper vessel at TU Darmstadt.
Yet the detector's assembly has to be finished. Until now, several parts still have to be produced and integrated. These are for example parts of the read-out electronics or the copper-braids that will connect the inner heat pipes with the Copper Cooling Mask. And of course, the FS pn-CCD has to be installed, tested and finally calibrated. For that, the software for the read-out of the present CCD will have to be adapted to the new system.
These tasks will probably take several months until the detector will be ready. Since the CAST experiment will be shut down in spring 2011, the chance that the new detector will take data for CAST is very small.
But there are other options: There might be future axion-searching experiments for which our detector could be very useful, as it is already optimized for usage in similar low background applications. Another option is to use it for very precise measurements of the response of the entrance window of pn-CCDs to electrons, which is very important for the future application of CCDs in space science like shown in the simulations for IXO.
There is exciting physics to be discovered.

8 Summary

In this thesis the first part of the construction of a new FS pn-CCD detector for low background applications such as CAST is described. An important motivation for this is the background reduction compared to the present CCD detector used at CAST. This reduction is achieved by integrating a Graded-Z Shield whose outer layers absorb high-energy X-rays while the inner layers absorb the fluorescence lines produced by the outer ones.
A simulation code for GEANT4 has been written in order to test the absorption and optimize the layer thicknesses of a Graded-Z Shield. Simulations have been carried out for the IXO Graded-Z but could be easily transferred to other shieldings like the one for the new detector.
In addition, the vacuum and cooling systems for the detector have been tested to verify their functionality for future applications.

A Cleaning Procedure

1. Brushing in 1:10 Tickopur R33 : pure H_2O
2. Rinsing with pure water
3. 10 min. cleaning in ultrasonic bath with 1:10 acetone : pure water
4. 10 min. cleaning in ultrasonic bath with some % Tickopur R33 in pure water
5. 10 min. cleaning in ultrasonic bath with pure water

After that storage in PE bags. As this is not optimal, components were later stored in a vacuum chamber at a pressure below $p < 1$ mbar and packed in aluminum foil for transport.

B Characteristics of some plastics

Table B.1.: Characteristics of different plastics: Data is taken from de.wikipedia.org and Goodfellow GmbH (www.goodfellow.com)

Material	**Density** [g/cm^3]	α_T [10^{-5}/K]	**Composition**	**lower working temp.** [^{o}C]	**Water absorption** [%]
HDPE	0.94	20	C_2H_4	-85	0.01
Kapton	1.42	3 - 6	$C_{22}H_{10}N_2O_5$	-270	2.8
PEEK	1.26 - 1.32	4.7	?	?	0.1 - 0.3
Polyamid 6.6	1.14	9.5	H,C,N,O	-30	2.5 - 3.1
PTFE	2.16	20	C_2F_4	-270	0.01

Stress tests for polyamide screws at low temperatures

The polyamide screws that are needed for the assembly of the detector are very small (M2x6 and M3x6). For the tests, bigger screws (M6x50) were used as they are easier to handle.
For the tests two sets each with ten screws were cooled and warmed several times using liquid nitrogen. After the cooling cycles the screws were jammed in a bench vise as seen in fig. B.1. Via a string the screw was pulled sidewards until it fractured or was deformed so far, that the measurement could not be continued. The occurring forces were measured with a spring scale.
Set 1 was cooled and heated 30 times. The screws were put under stress at room temperature.
Set 2 was cooled and heated 20 times. The screws were put under stress directly after removing them from the LN2 bath (within one minute).

Table B.2.: Results of the stress tests. A ">" indicates that the measurement could not be continued at a certain value because the screw was deformed to much.

Set 1		Set 2	
#	F [N]	#	F [N]
1	>35	1	24
2	>30	2	24
3	>30	3	>45
4	>35	4	30
5	>25	5	26
6	>25	6	24
7	>27	7	>37
8	>32	8	25
9	>26	9	22
10	>26	10	24

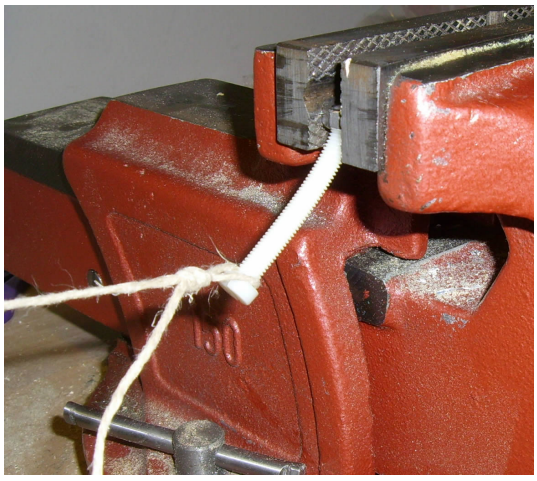

Figure B.1.: Setup for the stress test: The screws were jammed in a bench vise. The string is connected to a spring scale via a deflection roller.

All screws endured 22 N or more. None of the screws of set 1 fractured at all.
Taken into account the difference in the cross section and the length of the M2 screws compared to the M6 screws, the relation is as follows:

$$F_{M2\times6} = F_{M6\times50}\frac{l_{M6\times50}\cdot A_{M2\times6}}{l_{M2\times6}\cdot A_{M6\times50}} \tag{B.1}$$

With $r_{M6\times50} = 3\text{mm}$, $r_{M2\times6} = 1\text{mm}$, $l_{M6\times50} = 45\text{mm}$, $l_{M2\times6} = 6\text{mm}$ and $F_{M6\times50,max} = 20\text{N}$ one obtains

$$F_{M2\times6,max} = 16,66N.$$

Using Newton's Law $F = m \cdot g$, this roughly corresponds to a mass of 1.7 kg. This is about two orders of magnitude higher than the mass the screws have to bear.

C Simulation results

Appendix C gives a full overview of the data gained by the simulations of the Graded-Z Shield with varied thicknesses of the copper layers and the tantalum layers. The "standard" Graded-Z Shield used as a reference consists of the following layers: 0.1 mm C, 0.3 mm Al, 0.5 mm Cu, 2.2 mm Sn and 1,5 mm Ta.
All simulations have been run with 10^6 primary protons with an energy distribution as shown in fig. C.1.

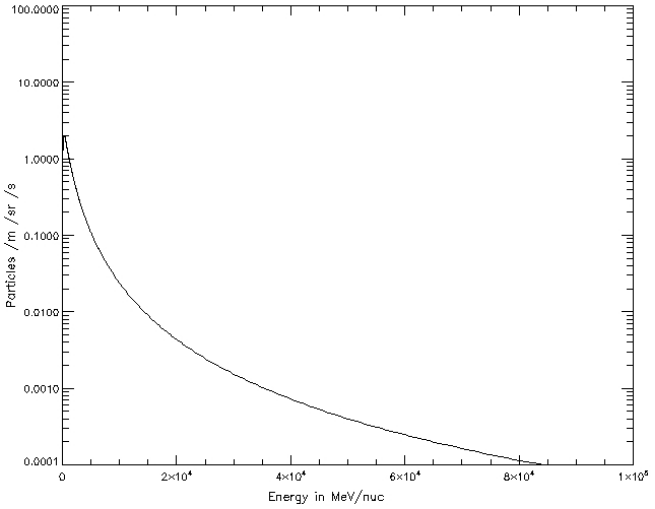

Figure C.1.: Proton input spectrum for the simulations derived from a CREME96 model.

Table C.1.: Counted gammas for simulations with different layers of tantalum and copper.

Ta thickness [mm]	**No. of Gammas**	**No. of Gammas <20 KeV**
0.0	11777	6433
0.5	15929	8548
1.0	19291	10250
1.5	21446	11472
2.0	25256	13253
2.5	26789	14184
Cu thickness [mm]		
0.5	11777	6433
1.434	15347	8304
2.368	17542	9550
3.302	20494	11145
4.236	22732	12278

Table C.2.: Counted electrons for simulations with different layers of tantalum and copper.

Ta thickness [mm]	**No. of electrons**	**No. of electrons <20 KeV**
0.0	565458	210308
0.5	598805	224228
1.0	617319	232143
1.5	642538	241968
2.0	659237	248688
2.5	674024	254170
Cu thickness [mm]		
0.5	565458	210308
1.434	603398	225948
2.368	619880	232379
3.302	638002	239856
4.236	658905	248240

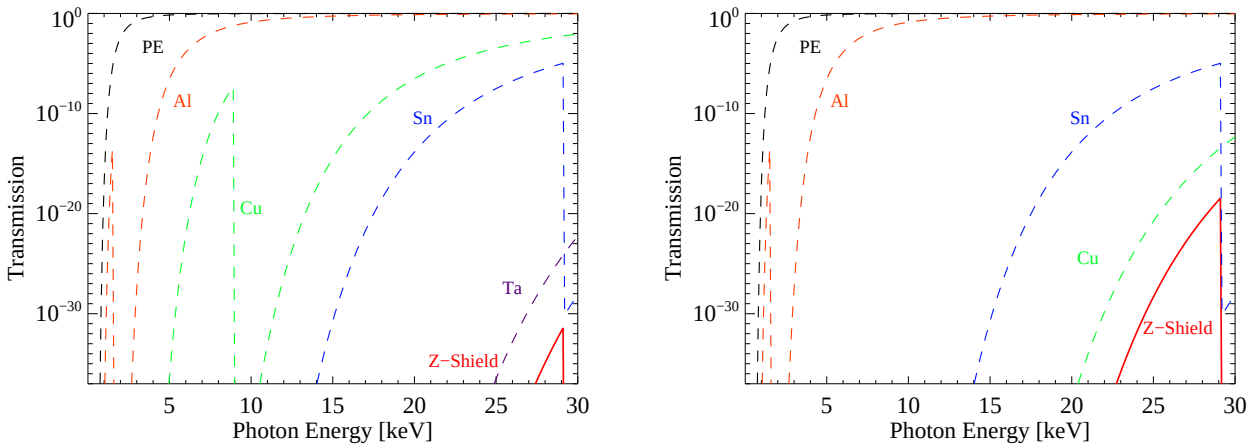

Figure C.2.: Left: The transmission of X-rays through Graded-Z Shield with the standard layers for IXO. Right: The transmission of X-rays through Graded-Z Shield with an increased copper thickness replacing th tantalum layer

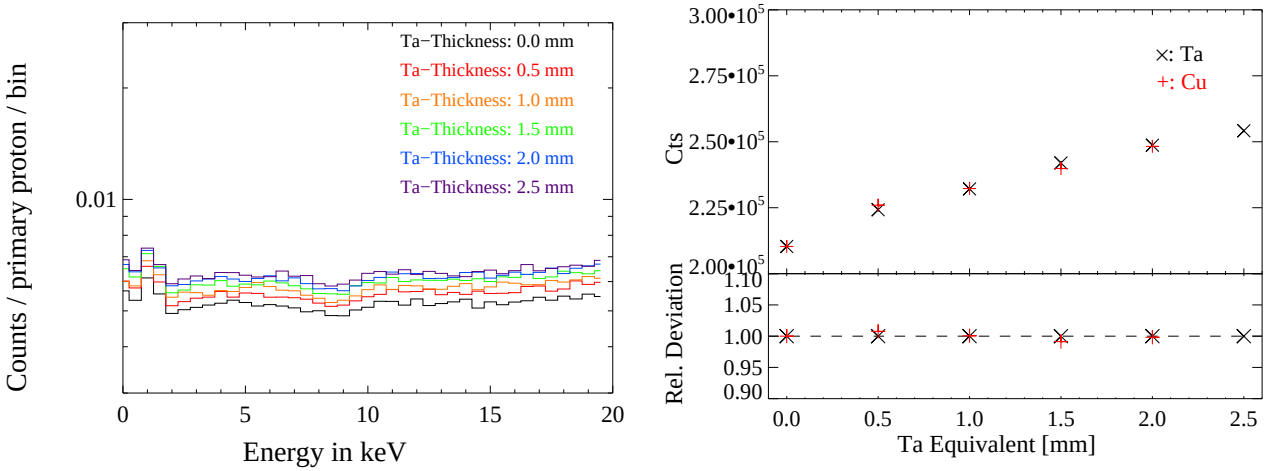

Figure C.3.: Left: The electron energy spectrum for a Graded-Z with tantalum layers of different thicknesses after irradiation with 10^6. The binsize is 0.5 keV. Right: A comparison of the number of counted gammas below 20 keV between simulations with tantalum and simulations with their density-equivalent in copper. The lower half of the plot shows the deviation of the counting rate with copper relative to tantalum. Errors have not been plotted as they would lie within the size of the symbols.

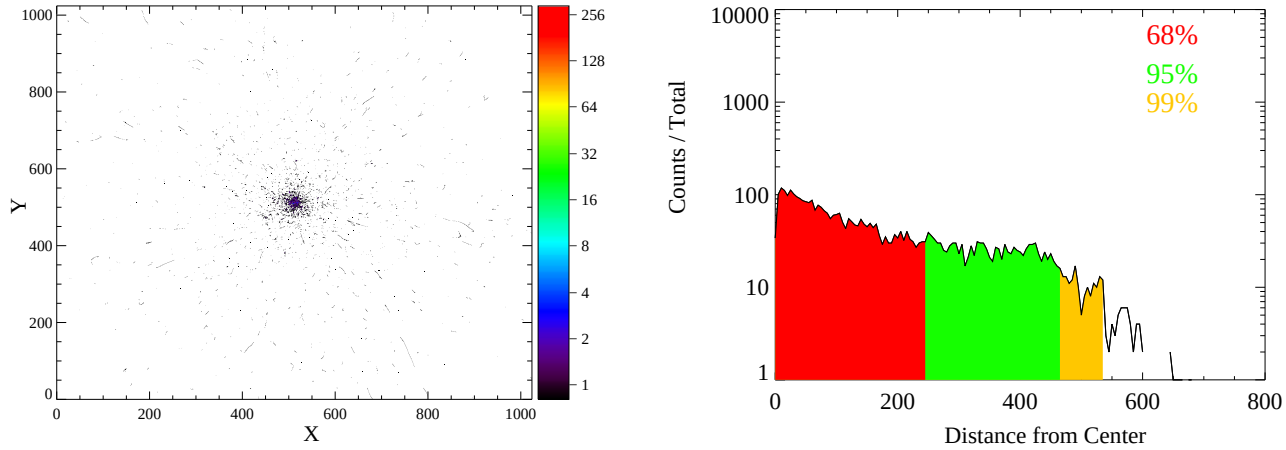

Figure C.4.: Left: The distribution of events caused by gammas on a Si-wafer with 1024×1024 pixels. Right: The distance of these events from the center of the chip, where the initial proton beam aims at. The coloured areas mark the distance that contains a certain percentage of all events.

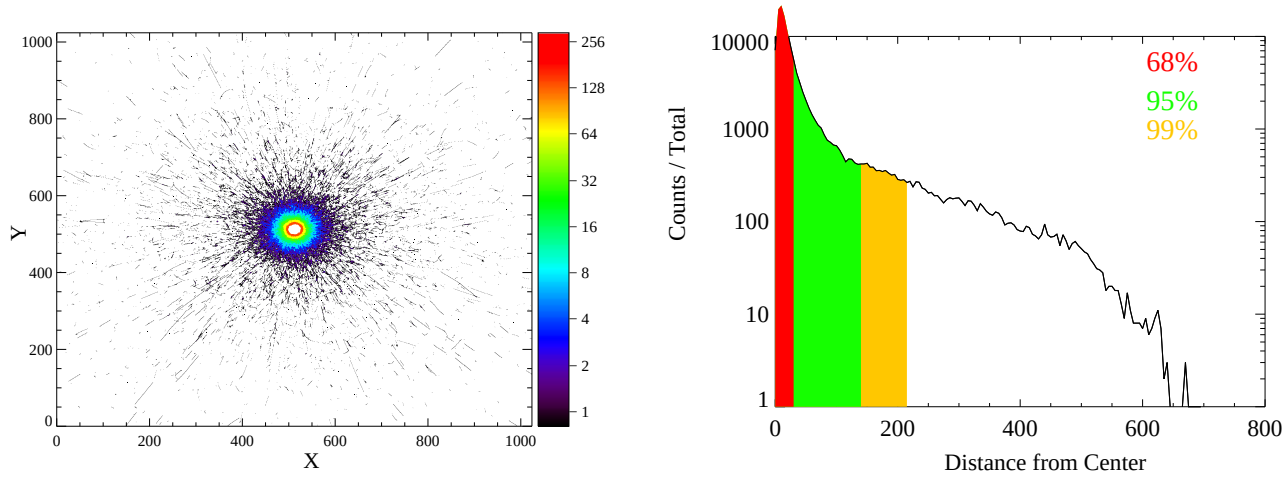

Figure C.5.: Left: The distribution of events caused by electrons on a Si-wafer with 1024×1024 pixels. Right: The distance of these events from the center of the chip, where the initial proton beam aims at. The coloured areas mark the distance that contains a certain percentage of all events.

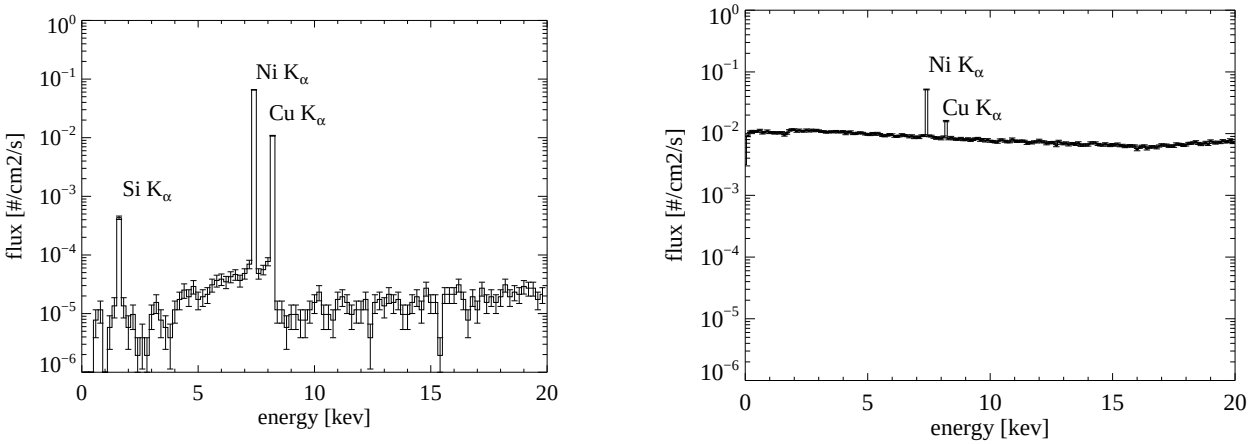

Figure C.6.: The gamma energy spectrum produced by gamma rays with an initial energy of 100 keV due to fluorescence emission of the following layering which is exemplary of a circuit board and casing near the detector: 3 mm Al, 0.3 mm Cu, 0.3 mm Si and 0.3 mm Ni. A Graded-Z Shield is not included. Left: Generated using the MULASSIS toolkit and showing only the gamma spectrum. One can clearly identify the Si-Kα, Cu-Kα and Ni-Kα lines. Right: Generated using our own simulation showing the summed gamma and electron spectrum. Both softwares compare well. One can see the importance of the electron component which envelops the Si-Kα line.

D Test results of the cooling system

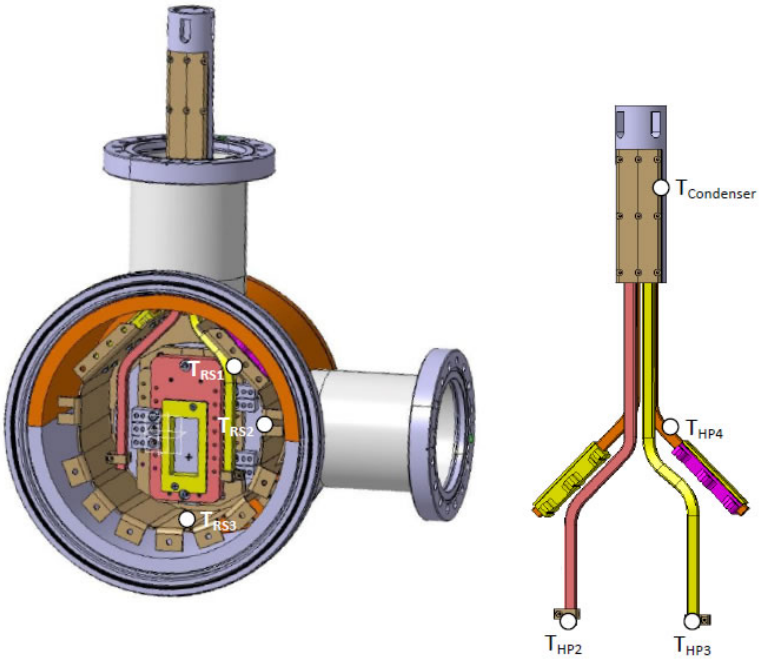

Figure D.1.: Placement of the temperature sensors for the measurements at CERN (Source: [22]).

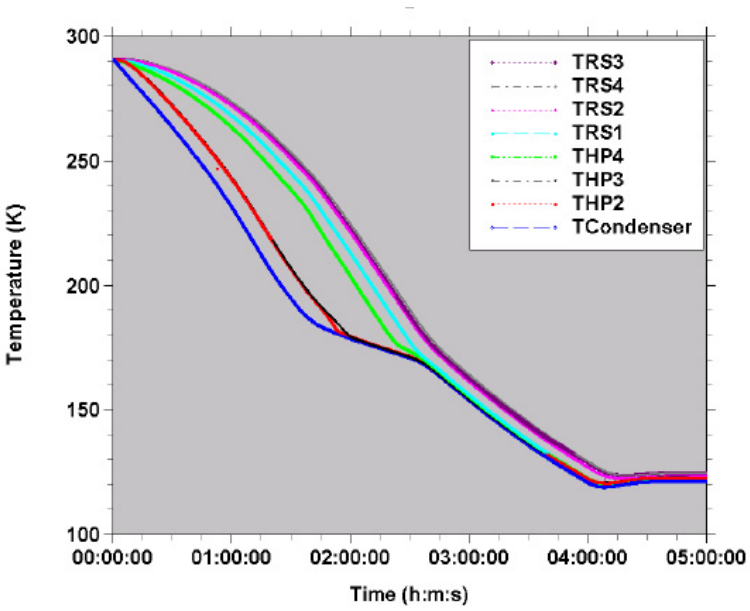

Figure D.2.: Cooldown temperatures measured at CERN in Feb. 2010 (Source: [22]).

Bibliography

[1] Abbon, P. ; Andriamonje, S. ; Aune, S. ; Dafni, T. ; Davenport, M. ; Delagnes, E. ; Oliveira, R. de ; Fanourakis, G. ; Ferrer Ribas, E. ; Franz, J. ; Geralis, T. ; Giganon, A. ; Gros, M. ; Giomataris, Y. ; Irastorza, I. G. ; Kousouris, K. ; Morales, J. ; Papaevangelou, T. ; Ruz, J. ; Zachariadou, K. ; Zioutas, K.: The Micromegas detector of the CAST experiment. In: *New J. Phys.* 9 (2007), Juni, S. 170–+. http://dx.doi.org/10.1088/1367-2630/9/6/170. – DOI 10.1088/1367–2630/9/6/170

[2] Agostinelli, S. ; Allison, J. ; Amako, K. ; Apostolakis, J. ; Araujo, H. ; Arce, P. ; Asai, M. ; Axen, D. ; Banerjee, S. ; Barrand, G. ; Behner, F. ; Bellagamba, L. ; Boudreau, J. ; Broglia, L. ; Brunengo, A. ; Burkhardt, H. ; Chauvie, S. ; Chuma, J. ; Chytracek, R. ; Cooperman, G. ; Cosmo, G. ; Degtyarenko, P. ; dell'Acqua, A. ; Depaola, G. ; Dietrich, D. ; Enami, R. ; Feliciello, A. ; Ferguson, C. ; Fesefeldt, H. ; Folger, G. ; Foppiano, F. ; Forti, A. ; Garelli, S. ; Giani, S. ; Giannitrapani, R. ; Gibin, D. ; Gómez Cadenas, J. J. ; González, I. ; Gracia Abril, G. ; Greeniaus, G. ; Greiner, W. ; Grichine, V. ; Grossheim, A. ; Guatelli, S. ; Gumplinger, P. ; Hamatsu, R. ; Hashimoto, K. ; Hasui, H. ; Heikkinen, A. ; Howard, A. ; Ivanchenko, V. ; Johnson, A. ; Jones, F. W. ; Kallenbach, J. ; Kanaya, N. ; Kawabata, M. ; Kawabata, Y. ; Kawaguti, M. ; Kelner, S. ; Kent, P. ; Kimura, A. ; Kodama, T. ; Kokoulin, R. ; Kossov, M. ; Kurashige, H. ; Lamanna, E. ; Lampén, T. ; Lara, V. ; Lefebure, V. ; Lei, F. ; Liendl, M. ; Lockman, W. ; Longo, F. ; Magni, S. ; Maire, M. ; Medernach, E. ; Minamimoto, K. ; Freitas, P. Mora d. ; Morita, Y. ; Murakami, K. ; Nagamatu, M. ; Nartallo, R. ; Nieminen, P. ; Nishimura, T. ; Ohtsubo, K. ; Okamura, M. ; O'Neale, S. ; Oohata, Y. ; Paech, K. ; Perl, J. ; Pfeiffer, A. ; Pia, M. G. ; Ranjard, F. ; Rybin, A. ; Sadilov, S. ; Salvo, E. di ; Santin, G. ; Sasaki, T. ; Savvas, N. ; Sawada, Y. ; Scherer, S. ; Sei, S. ; Sirotenko, V. ; Smith, D. ; Starkov, N. ; Stoecker, H. ; Sulkimo, J. ; Takahata, M. ; Tanaka, S. ; Tcherniaev, E. ; Safai Tehrani, E. ; Tropeano, M. ; Truscott, P. ; Uno, H. ; Urban, L. ; Urban, P. ; Verderi, M. ; Walkden, A. ; Wander, W. ; Weber, H. ; Wellisch, J. P. ; Wenaus, T. ; Williams, D. C. ; Wright, D. ; Yamada, T. ; Yoshida, H. ; Zschiesche, D.: Geant4- A Simulation Toolkit. 506 (2003), Juli, 250-303. http://www.cern.ch/geant4

[3] Altmann, J. ; Egle, W. J. ; Bingel, U. ; Hafner, W. ; Gänswein, B. ; Schwarz, H. ; Neugschwender, A.: Mirror system for the German X-Ray satellite ABRIXAS: I. Flight mirror fabrication, integration, and testing, S. 350–358

[4] Andriamonje, S. ; Aune, S. ; Barth, K. ; Belov, A. ; Beltrán, B. ; Bräuninger, H. ; Carmona, J. ; Cebrián, S. ; Collar, J. I. ; Dafni, T. ; Davenport, M. ; Di Lella, L. ; Eleftheriadis, C. ; Englhauser, J. ; Fanourakis, G. ; Ferrer-Ribas, E. ; Fischer, H. ; Franz, J. ; Friedrich, P. ; Geralis, T. ; Giomataris, I. ; Gninenko, S. ; Gómez, H. ; Hasinoff, M. ; Heinsius, F. H. ; Hoffmann, D. H. H. ; Irastorza, I. G. ; Jacoby, J. ; Jakovčić, K. ; Kang, D. ; Königsmann, K. ; Kotthaus, R. ; Krčmar, M. ; Kousouris, K. ; Kuster, M. ; Lakić, B. ; Lasseur, C. ; Liolios, A. ; Ljubičić, A. ; Lutz, G. ; Luzón, G. ; Miller, D. ; Morales, A. ; Morales, J. ; Ortiz, A. ; Papaevangelou, T. ; Placci, A. ; Raffelt, G. ; Riege, H. ; Rodríguez, A. ; Ruz, J. ; Savvidis, I. ;

SEMERTZIDIS, Y. ; SERPICO, P. ; STEWART, L. ; VILLAR, J. ; VOGEL, J. ; WALCKIERS, L. ; ZIOUTAS, K.: An improved limit on the axion-photon coupling from CAST. In: *J. Cosmol. Astropart. Phys.* 4 (2007), April, S. 10. http://dx.doi.org/doi:10.1088/1475-7516/2007/04/010. – DOI doi:10.1088/1475–7516/2007/04/010

[5] ASANO, Y. ; KIKUTANI, E. ; KUROKAWA, S. ; MIYACHI, T. ; MIYAJIMA, M. ; NAGASHIMA, Y. ; SHINKAWA, T. ; SUGIMOTO, S. ; YOSHIMURA, Y.: Search for a rare decay mode $K^+ \rightarrow \pi^+ \nu \overline{\nu}$ and axion. In: *Physics Letters B* 107 (1981), Nr. 1-2, 159 - 162. http://dx.doi.org/DOI:10.1016/0370-2693(81)91172-2. – DOI DOI: 10.1016/0370–2693(81)91172–2. – ISSN 0370–2693

[6] BAHCALL, J. N. ; PINSONNEAULT, M. H.: What Do We (Not) Know Theoretically about Solar Neutrino Fluxes ? 92 (2004), März, Nr. 12, S. 121301–+

[7] BAKER, C. A. ; DOYLE, D. D. ; GELTENBORT, P. ; GREEN, K. ; GRINTEN, M. G. D. d. ; HARRIS, P. G. ; IAYDJIEV, P. ; IVANOV, S. N. ; MAY, D. J. R. ; PENDLEBURY, J. M. ; RICHARDSON, J. D. ; SHIERS, D. ; SMITH, K. F.: An Improved Experimental Limit on the Electric Dipole Moment of the Neutron. In: *Phys. Rev. Lett.* 97 (2006), Februar, S. 131801

[8] BIBBER, K. van ; MCINTYRE, P. M. ; MORRIS, D. E. ; RAFFELT, G. G.: Design for a practical laboratory detector for solar axions. 39 (1989), April, S. 2089–2099

[9] CEBRIÁN, S. ; RODRÍGUEZ, A. ; KUSTER, M. ; BELTRÁN, B. ; GÓMEZ, H. ; HARTMANN, R. ; IRASTORZA, I. G. ; KOTTHAUS, R. ; LUZÓN, G. ; MORALES, J. ; RUZ, J. ; STRÜDER, L. ; VILLAR, J. A.: Background study for the pn-CCD detector of CERN Axion Solar Telescope. In: *Astroparticle Physics* 28 (2007), Oktober, S. 205–215. http://dx.doi.org/10.1016/j.astropartphys.2007.05.006. – DOI 10.1016/j.astropartphys.2007.05.006

[10] CHRISTENSON, J. H. ; CRONIN, J. W. ; FITCH, V. L. ; TURLAY, R.: Evidence for the 2 pi Decay of the k(2)0 Meson. In: *Phys. Rev. Lett.* 13 (1964), S. 138–140. http://dx.doi.org/10.1103/PhysRevLett.13.138. – DOI 10.1103/PhysRevLett.13.138

[11] GRUPEN, C. ; SHWARTZ, B.: *Particle Detectors (Cambridge Monographs on Particle Physics, Nuclear Physics and Cosmology)*. Cambridge University Press, 2008 http://www.worldcat.org/isbn/0521840066. – ISBN 0521840066

[12] HAUF, S.: *private communication*

[13] HAUF, S.: *Simulation on the SIMBOL-X Detector Background*, TU Darmstadt, Diplomarbeit, März 2009

[14] HAUF, S. ET AL.: Progress and Validation of Geant4 Based Radioactive Decay Simulation Using the Examples of Simbol-X and IXO, 2009. – IEEE Nuclear Science Symposium and Medical Imaging Conference, Orlando

[15] HEUSSER, G.: Low-Radioactivity Background Techniques. 45 (1995), S. 543–590

[16] KNOLL, G. F.: *Radiation detection and measurement*. 3rd. 605 Third Avenue, New York, NY 10158-0012 : New York, John Wiley & Sons, Inc., 2000

[17] Kuster, M. ; Bräuninger, H. ; Cebrián, S. ; Davenport, M. ; Eleftheriadis, C. ; Englhauser, J. ; Fischer, H. ; Franz, J. ; Friedrich, P. ; Hartmann, R. ; Heinsius, F. H. ; Hoffmann, D. H. H. ; Hoffmeister, G. ; Joux, J. N. ; Kang, D. ; Königsmann, K. ; Kotthaus, R. ; Papaevangelou, T. ; Lasseur, C. ; Lippitsch, A. ; Lutz, G. ; Morales, J. ; Rodríguez, A. ; Strüder, L. ; Vogel, J. ; Zioutas: The X-ray Telescope of CAST. In: *New J. Phys.* 9 (2007), Juni, S. 169–+. http://dx.doi.org/10.1088/1367-2630/9/6/169. – DOI 10.1088/1367–2630/9/6/169

[18] Marshall Space Flight Center: *Chandra X-ray Observatory Quick Facts*. http://www.nasa.gov/centers/marshall/news/background/facts/cxoquick.html. Version: 1999. – FS-1999-09-111-MSFC

[19] Meidinger, N. ; Andritschke, R. ; Hälker, O. ; Hartmann, R. ; Herrmann, S. ; Holl, P. ; Lutz, G. ; Kimmel, N. ; Schaller, G. ; Schnecke, M. ; Schopper, F. ; Soltau, H. ; Strüder, L.: Next generation of pnCCDs for X-ray spectroscopy and imaging. In: *Nuclear Instruments and Methods in Physics Research Section A: Accelerators, Spectrometers, Detectors and Associated Equipment* 568 (2006), Nr. 1, 141 - 148. http://dx.doi.org/DOI:10.1016/j.nima.2006.05.268. – DOI DOI: 10.1016/j.nima.2006.05.268. – ISSN 0168–9002. – New Developments in Radiation Detectors - Proceedings of the 10th European Symposium on Semiconductor Detectors, 10th European Symposium on Semiconductor Detectors

[20] Nordt, A.: *Suche nach Solaren Axionen mit dem Röntgenteleskop des CAST Experiments (Phase II)*, TU Darmstadt, Diss., September 2008. – Doktorarbeit

[21] Peccei, R. D. ; Quinn, H. R.: CP Conservation in the Presence of Pseudoparticles. In: *Phys. Rev. Lett.* 38 (1977), Juni, Nr. 25, S. 1440–1443

[22] Pereira, H.: *Cooling System for the CAST Frame-store PN-CCD Detector*. 2010. – CAST internal report

[23] Primakoff, H.: Photo-Production of Neutral Mesons in Nuclear Electric Fields and the Mean Life of the Neutral Meson. In: *Phys. Rev.* 81 (1951), Mar, Nr. 5, S. 899. http://dx.doi.org/10.1103/PhysRev.81.899. – DOI 10.1103/PhysRev.81.899

[24] Riabzev, S.: *Stirling-Cycle Machine*. http://www.ricor.com/Index.asp?CategoryID=81. Version: 2002. – RICOR Cryogenic & Vacuum Systems

[25] Rodríguez, A. ; Beltrán, B. ; Cebrián, S. ; Gómez, H. ; Hartmann, R. ; Irastorza, I. G. ; Klose, C. ; Kuster, M. ; Luzón, G. ; Morales, J. ; Ruz, J. ; Strüder, L. ; Villar, J. A.: Background studies for the pn-CCD detector of CAST, 2007, S. 143–146

[26] Strüder, L.: High-resolution imaging X-ray spectrometers. In: *Nuclear Instruments and Methods in Physics Research Section A: Accelerators, Spectrometers, Detectors and Associated Equipment* 454 (2000), November, Nr. 1, S. 73–113. http://dx.doi.org/10.1016/S0168-9002(00)00811-1. – DOI 10.1016/S0168–9002(00)00811–1

[27] Strüder, L. ; Bräuninger, H. W. ; Meidinger, N. ; Pfeffermann, E. ; Hartmann, R. ; Reppin, C. ; Briel, U. G. ; Hippmann, H. ; Kink, W. ; Hauff, D. ; Krause, N. ; Aschenbach, B. ;

Hartner, G. ; Dennerl, K. ; Haberl, F. ; Stötter, S. ; Kemmer, S. ; Trümper, J. ; Lutz, G. ; Richter, R. H. ; Solc, P. ; Eckart, R. ; Kendziorra, E. ; Kuster, M. ; Zanthier, C. von ; Holl, P. ; Viehl, A. ; Kirsch, S. ; Kemmer, J. ; Soltau, H.: X-ray pn-CCDs on the XMM-Newton Observatory. Bellingham, WA : SPIE, 2000, S. 342–352

[28] Strüder, L. ; Briel, U. ; Dennerl, K. ; Hartmann, R. ; Kendziorra, E. ; Meidinger, N. ; Pfeffermann, E. ; Reppin, C. ; Aschenbach, B. ; Bornemann, W. ; Bräuninger, H. ; Burkert, W. ; Elender, M. ; Freyberg, M. ; Haberl, F. ; Hartner, G. ; Heuschmann, F. ; Hippmann, H. ; Kastelic, E. ; Kemmer, S. ; Kettenring, G. ; Kink, W. ; Krause, N. ; Müller, S. ; Oppitz, A. ; Pietsch, W. ; Popp, M. ; Predehl, P. ; Read, A. ; Stephan, K. H. ; Stötter, D. ; Trümper, J. ; Holl, P. ; Kemmer, J. ; Soltau, H. ; Stötter, R. ; Weber, U. ; Weichert, U. ; Zanthier, C. von ; Carathanassis, D. ; Lutz, G. ; Richter, R. H. ; Solc, P. ; Böttcher, H. ; Kuster, M. ; Staubert, R. ; Abbey, A. ; Holland, A. ; Turner, M. ; Balasini, M. ; Bignami, G. F. ; La Palombara, N. ; Villa, G. ; Buttler, W. ; Gianini, F. ; Lainé, R. ; Lumb, D. ; Dhez, P.: The European Photon Imaging Camera on XMM-Newton: The pn-CCD camera. 365 (2001), Januar, S. L18–L26. http://dx.doi.org/10.1051/0004-6361:20000066. – DOI 10.1051/0004–6361:20000066

[29] Thompson, A. C.: *X-ray data booklet*. 2nd. Technical Information Department, Lawrence Berkeley Laboratory, Berkeley, California 94720, 2001

[30] Tylka, A.J. ; Dietrich, W.F. ; Boberg, P.R. ; Smith, E.C. ; Adams, J.H. Jr. ; Brownstein, B ; Flueckinger, E.O. ; Petersen, E.L. ; M.A., Shea ; Smart, D.F.: CREME96: A Revision of the Cosmic Ray Effects on Micro-Electronics Code. (1997), S. 2150–2160

[31] Vogel, J.: *Searching for Solar Axions in the eV-Mass Region with the CCD Detector at CAST*, Universität Freiburg, Diss., April 2009. – Doktorarbeit

[32] Wolter, H.: Spiegelsysteme streifenden Einfalls als Abbildende Optiken für Röntgenstrahlen. In: *Ann. der Physik, VI. F.* 10 (1952), S. 94–114

[33] Zioutas, K. ; Aalseth, C. E. ; Abriola, D. ; F. T. A., I. ; Brodzinski, R. L. ; Collar, J. I. ; Creswick, R. ; Gregorio, D. E. D. ; Farach, H. ; Gattone, A. O. ; Guérard, C. K. ; Hasenbalg, F. ; Hasinoff, M. ; Huck, H. ; Liolios, A. ; Miley, H. S. ; Morales, A. ; Morales, J. ; Nikas, D. ; Nussinov, S. ; Ortiz, A. ; Savvidis, E. ; Scopel, S. ; Sievers, P. ; Villar, J. A. ; Walckiers, L.: A decommissioned LHC model magnet as an axion telescope. In: *Nucl. Instrum. Methods Phys. Res., Sect. A* 425 (1999), April, S. 480–487

[34] Zioutas, K. ; Hoffmann, D. H. H. ; Dennerl, K. ; Papaevangelou, T.: What is Dark Matter Made Of. 306 (2004), November, Nr. 5701, S. 1485–1488

Acknowledgements

Zuerst möchte ich mich bei Herrn Prof. D. H. H. Hoffmann bedanken, der mir die Möglichkeit gegeben hat, meine Master-Thesis über dieses Thema zu schreiben. Sein Rat war sehr wertvoll bei vielen Problemen.
Außerdem geht mein Dank an meinen Betreuer Dr. Markus Kuster, ohne den dieses Projekt wohl nie Zustande gekommen wäre. Er war - auch nach seinem Umzug nach Hamburg - eine treibende Kraft für die Entwicklung des FS-CCD Detektors. Von seinem außergewöhnlichen Fachwissen und seinen Tipps habe ich sehr profitiert.
Auch Steffen Hauf möchte ich danken für die gute Gesellschaft im Büro, seine ebenfalls hilfreichen Tipps und dafür, dass er auch mal mit angepackt hat, wenn es was zu tun gab. Auch den übrigen Mitgliedern der Arbeitsgruppe danke ich für die Hilfe und die allgemein angenehme Arbeitsatmosphäre. Auch den vielen anderen Leuten, die innerhalb und außerhalb der TU Darmstadt auf die eine oder andere Weise zur Entwicklung des Detektors und seiner Fertigstellung beigetragen haben, möchte ich danken. Insbesondere gilt dies auch für Herrn Häckl und seine Mitarbeiter aus der mechanischen Werkstatt, die mehrmals die letzte Rettung waren, wenn es handwerkliche Probleme gab.
Zum Schluss seien noch meine Familie und meine Freunde erwähnt, die mich immer unterstützt haben und auch mal abgelenkt, wenn ich den Kopf zu sehr voller Arbeit hatte. Ich danke euch.